A Paper Entitled

Effect of Crystal Orientation on Fatigue Failure of Single Crystal Nickel Base Turbine Blade Superalloys

Submitted for presentation in the

ASME TURBO EXPO 2000

The 45th ASME International Gas Turbine & Aeroengine Technical Congress, Exposition and Users Symposium
MUNICH, GERMANY
8-11 May 2000

And for publication in the *ASME Journal of Gas Turbines and Power*

By

Nagaraj K. Arakere
Associate Professor
Mechanical Engineering Department
University of Florida
Gainesville, FL 32611-6300

Gregory R. Swanson
NASA Marshall Space Flight Center
ED22/Strength Analysis Group
MSFC, Alabama-35812

Effect of Crystal Orientation on Fatigue Failure of Single Crystal Nickel Base Turbine Blade Superalloys

1.0 Introduction

High Cycle Fatigue (HCF) induced failures in aircraft gas-turbine engines is a pervasive problem affecting a wide range of components and materials. HCF is currently the primary cause of component failures in gas turbine aircraft engines [1]. Turbine blades in high performance aircraft and rocket engines are increasingly being made of single crystal nickel superalloys. Single-crystal Nickel-base superalloys were developed to provide superior creep, stress rupture, melt resistance and thermomechanical fatigue capabilities over polycrystalline alloys previously used in the production of turbine blades and vanes. Currently the most widely used single crystal turbine blade superalloys are PWA 1480/1493 and PWA 1484. These alloys play an important role in commercial, military and space propulsion systems. PWA1493, identical to PWA1480, but with tighter chemical constituent control, is used in the NASA SSME alternate turbopump, a liquid hydrogen fueled rocket engine.

Single-crystal materials differ significantly from polycrystalline alloys in that they have highly orthotropic properties making the position of the crystal lattice relative to the part geometry a significant factor in the overall analysis [2]. The modified Goodman approach currently used for component design does not address important factors that affect HCF such as fretting and/or galling surface damage, and interaction with LCF [1]. Rocket engine service presents another set of requirements that shifts emphasis to low temperature fatigue and fracture capability with particular attention given to thermal, cryogenic and high pressure hydrogen gas exposure [3]. To address HCF induced component failures, the gas turbine industry, NASA, the US Air Force, and the US Navy have made significant efforts in understanding fatigue in single-crystal turbine blade superalloys. Understanding fatigue initiation, threshold, and Region II fatigue crack growth are of primary importance and there is great need for improvements in fracture mechanics properties of turbine blade alloys. While a large amount of data has been collected there currently exists no simple method for applying this knowledge toward the design of more robust single crystal gas turbine engine components. It is therefore essential to develop failure criteria for single crystals, based on available fatigue and fracture test data that will permit a designer to utilize the lessons learned.

Objectives for this paper are motivated by the need for developing failure criteria and fatigue life evaluation procedures for high temperature single crystal components, using available fatigue data and finite element modeling of turbine blades. Fatigue failure criteria are developed for single crystal material by suitably modifying failure criteria for polycrystalline material. The proposed criteria are applied for uniaxial LCF test data, to determine the most effective failure parameter. A fatigue life equation is developed based on the curve fit of the failure parameter with LCF test data. Single crystal turbine blades used in the alternate advanced high-pressure fuel turbopump (AHPFTP/AT) are modeled using a large-scale 3D finite element (FE) model capable of accounting for material orthotrophy and variation in primary and secondary crystal orientation. Using the FE stress analysis results and the fatigue life relations developed, the effect of variation of primary and secondary crystal orientations on life is determined, at critical blade locations. The most advantageous crystal orientation for a given blade design is determined. Results presented demonstrates that control of secondary and primary crystallographic

orientation has the potential to optimize blade design by increasing its resistance to fatigue crack growth without adding additional weight or cost.

2.0 Crystal Orientation

Nickel based single-crystal superalloys are precipitation strengthened cast mono grain superalloys based on the Ni-Cr-Al system. The microstructure consists of approximately 60% by volume of γ' precipitates in a γ matrix. The γ' precipitate, based on the intermetallic compound Ni_3Al, is the strengthening phase in nickel-base superalloys. The γ' precipitate is a Face Centered Cubic (FCC) structure and composed of the intermetallic compound Ni_3Al. The γ' precipitate is suspended within the γ matrix, which is also of FCC structure and comprised of nickel with cobalt, chromium, tungsten and tantalum in solution. Single crystal superalloys have highly orthotropic material properties that vary significantly with direction relative to the crystal lattice. Primary crystallographic orientation of a turbine blade, commonly referred to as α, is defined as the relative angle between the airfoil stacking line and the <001> direction, as shown in Fig. 1. Current manufacturing capability permits control of α to within $5°$ of the stacking line. Secondary orientation β defines the angle of the <100> orientation relative to the blade geometry. In most turbine blade castings the secondary orientation β is neither specified nor controlled during the manufacturing process. The β orientation for a given blade casting therefore becomes a random variable. Usually, however, the β orientation for each blade is recorded after the casting process is complete.

3.0 Fatigue in Single Crystal Nickel Superalloys

Slip in metal crystals often occurs on planes of high atomic density in closely packed directions. The 4 octahedral planes corresponding to the high-density planes in the FCC crystal are shown in Fig. 2. Each octahedral plane has 6 slip directions associated with it. Three of these are termed easy-slip or primary slip directions and the other 3 are secondary slip directions. Thus there are 12 primary and 12 secondary slip directions associated with the 4 octahedral planes [4]. In addition, there are 6 possible slip directions in the three cube planes, as shown in Fig. 3. Deformation mechanisms operative in PWA 1480/1493 are divided into three-temperature regions [5]. In the low temperature regime (26C to 427C, 79F to 800F)) the principal deformation mechanism is by (111)/<110> slip, and hence fractures produced at these temperatures exhibit (111) facets. Above 427C (800F) thermally activated cube cross slip is observed which is manifested by an increasing yield strength up to 871C (1600F) and a proportionate increase in (111) dislocations that have cross slipped to (001) planes. Thus nickel based FCC single crystal superalloys slip primarily on the octahedral and cube planes in specific slip directions. At low temperature and stress conditions crystallographic initiation appears to be the most prevalent mode. This mode warrants special consideration since this mode of cracking has been observed in many turbine blade failures [3]. The operative deformation mechanism has a strong influence on the nature of fracture. As a result of the two phase microstructure present in single crystal nickel alloys a complex set of fracture mode exists based on the dislocation motion in the matrix (γ) and precipitate phase (γ'). Telesman and Ghosn [6] have observed the transition of fracture mode as a function of stress intensity (K) in PWA1480 at room temperature. Deluca and Cowles [7] have observed the fracture mode transition that is environmentally dependent.

Fatigue life estimation of single crystal blade components represents an important aspect of durability assessment. Turbine blade material is subjected to large mean stresses from the centrifugal stress field. High frequency alternating fatigue stresses are a function of the vibratory characteristics of the blade. Any fatigue failure criteria chosen must have the ability to account for high mean stress effects. Towards identifying fatigue failure criteria for single crystal material we consider four fatigue failure theories used for polycrystalline material subjected to multiaxial states of fatigue stress. Kandil, et al [8] presented a shear and normal strain based model, shown in Eq. 1, based on the critical plane approach which postulates that cracks initiate and grow on certain planes and that the normal strains to those planes assist in the fatigue crack growth process. In Eq. (1) γ_{max} is the max shear strain on the critical plane, ε_n the normal strain on the same plane, S is a constant, and N is the cycles to initiation.

$$\gamma_{max} + S\,\varepsilon_n = f(N) \tag{1}$$

Socie, et al [9] presented a modified version of this theory shown in Eq. (2), to include mean stress effects. Here the maximum shear strain amplitude $(\Delta\gamma)$ is modified by the normal strain amplitude $(\Delta\varepsilon)$ and the mean stress normal to the maximum shear strain amplitude (σ_{no}).

$$\frac{\Delta\gamma}{2} + \frac{\Delta\varepsilon_n}{2} + \frac{\sigma_{no}}{E} = f(N) \tag{2}$$

Fatemi and Socie [10] have presented an alternate shear based model for multiaxial mean-stress loading that exhibits substantial out-of-phase hardening, shown in Eq. (3). This model indicates that no shear direction crack growth occurs if there is no shear alternation.

$$\frac{\Delta\gamma}{2}\left(1 + k\frac{\sigma_n^{max}}{\sigma_y}\right) = f(N) \tag{3}$$

Smith, et al [11] proposed a uniaxial parameter to account for mean stress effects which was modified for multiaxial loading, shown in Eq. (4), by Bannantine and Socie [12]. Here the maximum principal strain amplitude is modified by the maximum stress in the direction of maximum principal strain amplitude that occurs over one cycle.

$$\frac{\Delta\varepsilon_1}{2}(\sigma^{max}) = f(N) \tag{4}$$

4.0 Application of Failure Criteria to Uniaxial LCF Test Data

The polycrystalline failure parameters described by Eqs. (1-4) will be applied for single crystal uniaxial strain controlled LCF test data. Transformation of the stress and strain tensors between the material and specimen coordinate systems (Fig. 4) is necessary for implementing the failure theories outlined. The components of stresses and strains in the (x', y', z') system in terms of the (x, y, z) system is given by [13]

$$\{\sigma'\} = [Q']\{\sigma\} \; ; \quad \{\varepsilon'\} = [Q'_\varepsilon]\{\varepsilon\} \tag{5}$$

$$\{\sigma\} = [Q']^{-1}\{\sigma'\} = [Q]\{\sigma'\}; \; \{\varepsilon\} = [Q'_\varepsilon]^{-1}\{\varepsilon'\} = [Q_\varepsilon]\{\varepsilon'\} \tag{6}$$

Where

$$\{\sigma'\} = \begin{Bmatrix} \sigma'_x \\ \sigma'_y \\ \sigma'_z \\ \tau'_{yz} \\ \tau'_{zx} \\ \tau'_{xy} \end{Bmatrix} \quad , \quad \{\sigma\} = \begin{Bmatrix} \sigma_x \\ \sigma_y \\ \sigma_z \\ \tau_{yz} \\ \tau_{zx} \\ \tau_{xy} \end{Bmatrix} \quad ; \quad \{\varepsilon'\} = \begin{Bmatrix} \varepsilon'_x \\ \varepsilon'_y \\ \varepsilon'_z \\ \gamma'_{yz} \\ \gamma'_{zx} \\ \gamma'_{xy} \end{Bmatrix} \quad and \quad \{\varepsilon\} = \begin{Bmatrix} \varepsilon_x \\ \varepsilon_y \\ \varepsilon_z \\ \gamma_{yz} \\ \gamma_{zx} \\ \gamma_{xy} \end{Bmatrix} \tag{7}$$

$$[Q] = \begin{bmatrix} \alpha_1^2 & \alpha_2^2 & \alpha_3^2 & 2\alpha_3\alpha_2 & 2\alpha_1\alpha_3 & 2\alpha_2\alpha_1 \\ \beta_1^2 & \beta_2^2 & \beta_3^2 & 2\beta_3\beta_2 & 2\beta_1\beta_3 & 2\beta_2\beta_1 \\ \gamma_1^2 & \gamma_2^2 & \gamma_3^2 & 2\gamma_3\gamma_2 & 2\gamma_1\gamma_3 & 2\gamma_2\gamma_1 \\ \beta_1\gamma_1 & \beta_2\gamma_2 & \beta_3\gamma_3 & (\beta_2\gamma_3 + \beta_3\gamma_2) & (\beta_1\gamma_3 + \beta_3\gamma_1) & (\beta_1\gamma_2 + \beta_2\gamma_1) \\ \gamma_1\alpha_1 & \gamma_2\alpha_2 & \gamma_3\alpha_3 & (\gamma_2\alpha_3 + \gamma_3\alpha_2) & (\gamma_1\alpha_3 + \gamma_3\alpha_1) & (\gamma_1\alpha_2 + \gamma_2\alpha_1) \\ \alpha_1\beta_1 & \alpha_2\beta_2 & \alpha_3\beta_3 & (\alpha_2\beta_3 + \alpha_3\beta_2) & (\alpha_1\beta_3 + \alpha_3\beta_1) & (\alpha_1\beta_2 + \alpha_2\beta_1) \end{bmatrix} \tag{8}$$

and

$$[Q_\varepsilon] = \begin{bmatrix} \alpha_1^2 & \alpha_2^2 & \alpha_3^2 & \alpha_3\alpha_2 & \alpha_1\alpha_3 & \alpha_2\alpha_1 \\ \beta_1^2 & \beta_2^2 & \beta_3^2 & \beta_3\beta_2 & \beta_1\beta_3 & \beta_2\beta_1 \\ \gamma_1^2 & \gamma_2^2 & \gamma_3^2 & \gamma_3\gamma_2 & \gamma_1\gamma_3 & \gamma_2\gamma_1 \\ 2\beta_1\gamma_1 & 2\beta_2\gamma_2 & 2\beta_3\gamma_3 & (\beta_2\gamma_3 + \beta_3\gamma_2) & (\beta_1\gamma_3 + \beta_3\gamma_1) & (\beta_1\gamma_2 + \beta_2\gamma_1) \\ 2\gamma_1\alpha_1 & 2\gamma_2\alpha_2 & 2\gamma_3\alpha_3 & (\gamma_2\alpha_3 + \gamma_3\alpha_2) & (\gamma_1\alpha_3 + \gamma_3\alpha_1) & (\gamma_1\alpha_2 + \gamma_2\alpha_1) \\ 2\alpha_1\beta_1 & 2\alpha_2\beta_2 & 2\alpha_3\beta_3 & (\alpha_2\beta_3 + \alpha_3\beta_2) & (\alpha_1\beta_3 + \alpha_3\beta_1) & (\alpha_1\beta_2 + \alpha_2\beta_1) \end{bmatrix} \tag{9}$$

Table 1 shows the direction cosines between the (x, y, z) and (x', y', z') coordinate axes. The transformation matrix $[Q]$ is orthogonal and hence $[Q]^{-1} = [Q]^T = [Q']$. The generalized Hooke's law for a homogeneous anisotropic body in Cartesian coordinates (x, y, z) is given by Eq. (10) [13].

$$\{\varepsilon\} = [a_{ij}]\{\sigma\} \tag{10}$$

$[a_{ij}]$ is the matrix of 36 elastic coefficients, of which only 21 are independent, since $[a_{ij}] = [a_{ji}]$. The elastic properties of FCC crystals exhibit cubic symmetry, also described as cubic syngony. Materials with cubic symmetry have only three independent elastic constants designated as the elastic modulus, shear modulus, and Poisson ratio [4] and hence $[a_{ij}]$ has only 3 independent elastic constants, as given below.

$$[a_{ij}] = \begin{bmatrix} a_{11} & a_{12} & a_{12} & 0 & 0 & 0 \\ a_{12} & a_{11} & a_{12} & 0 & 0 & 0 \\ a_{12} & a_{12} & a_{11} & 0 & 0 & 0 \\ 0 & 0 & 0 & a_{44} & 0 & 0 \\ 0 & 0 & 0 & 0 & a_{44} & 0 \\ 0 & 0 & 0 & 0 & 0 & a_{44} \end{bmatrix} \qquad (12)$$

The elastic constants are

$$a_{11} = \frac{1}{E_{xx}}, \; a_{44} = \frac{1}{G_{yz}}, \; a_{12} = -\frac{v_{yx}}{E_{xx}} = -\frac{v_{xy}}{E_{yy}} \qquad (13)$$

The elastic constants in the generalized Hooke's law of an anisotropic body, $[a_{ij}]$, vary with the direction of the coordinate axes. In the case of an isotropic body the constants are invariant in any orthogonal coordinate system. The elastic constant matrix $[a'_{ij}]$ in the (x', y', z') coordinate system that relates $\{\varepsilon'\}$ and $\{\sigma'\}$ is given by the following transformation [13].

$$[a'_{ij}] = [Q]^T [a_{ij}][Q] = \sum_{m=1}^{6} \sum_{n=1}^{6} a_{mn} Q_{mi} Q_{nj} \qquad (14)$$

$$(i, j = 1, 2, \ldots\ldots, 6)$$

Shear stresses in the 30 slip systems shown in figures 1 and 2 are denoted by τ^1, τ^2,..., τ^{30}. The shear stresses on the 24 octahedral slip systems are [4]

$$\begin{Bmatrix} \tau^1 \\ \tau^2 \\ \tau^3 \\ \tau^4 \\ \tau^5 \\ \tau^6 \\ \tau^7 \\ \tau^8 \\ \tau^9 \\ \tau^{10} \\ \tau^{11} \\ \tau^{12} \end{Bmatrix} = \frac{1}{\sqrt{6}} \begin{bmatrix} 1 & 0 & -1 & 1 & 0 & -1 \\ 0 & -1 & 1 & -1 & 1 & 0 \\ 1 & -1 & 0 & 0 & 1 & -1 \\ -1 & 0 & 1 & 1 & 0 & -1 \\ -1 & 1 & 0 & 0 & -1 & -1 \\ 0 & 1 & -1 & -1 & -1 & 0 \\ 1 & -1 & 0 & 0 & -1 & -1 \\ 0 & 1 & -1 & -1 & 1 & 0 \\ 1 & 0 & -1 & -1 & 0 & -1 \\ 0 & -1 & 1 & -1 & -1 & 0 \\ -1 & 0 & 1 & -1 & 0 & -1 \\ -1 & 1 & 0 & 0 & 1 & -1 \end{bmatrix} \begin{Bmatrix} \sigma_{xx} \\ \sigma_{yy} \\ \sigma_{zz} \\ \sigma_{xy} \\ \sigma_{zx} \\ \sigma_{yz} \end{Bmatrix}, \; \begin{Bmatrix} \tau^{13} \\ \tau^{14} \\ \tau^{15} \\ \tau^{16} \\ \tau^{17} \\ \tau^{18} \\ \tau^{19} \\ \tau^{20} \\ \tau^{21} \\ \tau^{22} \\ \tau^{23} \\ \tau^{24} \end{Bmatrix} = \frac{1}{3\sqrt{2}} \begin{bmatrix} -1 & 2 & -1 & 1 & -2 & 1 \\ 2 & -1 & -1 & 1 & 1 & -2 \\ -1 & -1 & 2 & -2 & 1 & 1 \\ -1 & 2 & -1 & -1 & -2 & -1 \\ -1 & -1 & 2 & 2 & 1 & -1 \\ 2 & -1 & -1 & -1 & 1 & 2 \\ -1 & -1 & 2 & 2 & -1 & 1 \\ 2 & -1 & -1 & -1 & -1 & -2 \\ -1 & 2 & -1 & -1 & 2 & 1 \\ 2 & -1 & -1 & 1 & -1 & 2 \\ -1 & 2 & -1 & 1 & 2 & -1 \\ -1 & -1 & 2 & -2 & -1 & -1 \end{bmatrix} \begin{Bmatrix} \sigma_{xx} \\ \sigma_{yy} \\ \sigma_{zz} \\ \sigma_{xy} \\ \sigma_{zx} \\ \sigma_{yz} \end{Bmatrix}$$

$$(15)$$

and the shear stresses on the 6 cube slip systems are

$$\begin{Bmatrix} \tau^{25} \\ \tau^{26} \\ \tau^{27} \\ \tau^{28} \\ \tau^{29} \\ \tau^{30} \end{Bmatrix} = \frac{1}{\sqrt{2}} \begin{bmatrix} 0 & 0 & 0 & 1 & 1 & 0 \\ 0 & 0 & 0 & 1 & -1 & 0 \\ 0 & 0 & 0 & 1 & 0 & 1 \\ 0 & 0 & 0 & 1 & 0 & -1 \\ 0 & 0 & 0 & 0 & 1 & 1 \\ 0 & 0 & 0 & 0 & -1 & 1 \end{bmatrix} \begin{Bmatrix} \sigma_{xx} \\ \sigma_{yy} \\ \sigma_{zz} \\ \sigma_{xy} \\ \sigma_{zx} \\ \sigma_{yz} \end{Bmatrix} \qquad (16)$$

Shear strains (engineering) on the 30 slip systems are calculated using similar kinematic relations.

As an example problem we consider a uniaxial test specimen loaded in the [213] direction (chosen as the x' axis in Fig. 4) under strain control. The applied strain for the specimen is 1.212 %. We wish to calculate the stresses and strains in the material coordinate system and the shear stresses on the 30 slip systems. The x' axis is aligned along the [213] direction. The required direction cosines are shown in Table 2. The stress-strain relationship in the specimen coordinate system is given by

$$\{\varepsilon'\} = [a'_{ij}]\{\sigma'\} \qquad (17)$$

The $[a'_{ij}]$ matrix is calculated using Eq. (14).

$$[a'_{ij}] = \begin{bmatrix} 3.537E-8 & -2.644E-9 & -1.986E-8 & 5.209E-9 & 1.405E-8 & 1.878E-8 \\ -2.644E-9 & 3.975E-8 & -2.423E-8 & -5.61E-9 & 1.297E-8 & -2.023E-8 \\ -1.986E-8 & -2.423E-8 & 5.696E-8 & 4.007E-10 & -2.703E-8 & 1.445E-9 \\ 5.209E-9 & -5.61E-9 & 4.007E-10 & 7.089E-8 & 2.889E-9 & 2.595E-8 \\ 1.405E-8 & 1.297E-8 & -2.703E-8 & 2.889E-9 & 8.838E-8 & 1.042E-8 \\ 1.878E-8 & -2.023E-8 & 1.445E-9 & 2.595E-8 & 1.042E-8 & 1.572E-7 \end{bmatrix}$$

$$(18)$$

Since σ_x` is the only nonzero stress in the specimen coordinate system, we have

$$\sigma'_x = \frac{\varepsilon'_x}{a'_{11}} = \frac{0.01212}{3.537E-8} = 342{,}663 \, psi \qquad (19)$$

Knowing $\{\sigma'\}$ we can now calculate $\{\varepsilon'\}$ as

$$\{\varepsilon'\} = \begin{Bmatrix} \varepsilon'_x \\ \varepsilon'_y \\ \varepsilon'_z \\ \gamma'_{yz} \\ \gamma'_{zx} \\ \gamma'_{xy} \end{Bmatrix} = [a'_{ij}] \begin{Bmatrix} 342{,}663 \\ 0 \\ 0 \\ 0 \\ 0 \\ 0 \end{Bmatrix} = \begin{Bmatrix} 0.01212 \\ -9.059E-4 \\ -6.805E-3 \\ 1.785E-3 \\ 4.815E-3 \\ 6.435E-3 \end{Bmatrix} \qquad (20)$$

The stresses and strains in the material coordinate system can be calculated using Eqs. (6) as

$$
\begin{Bmatrix} \varepsilon_x \\ \varepsilon_y \\ \varepsilon_z \\ \gamma_{yz} \\ \gamma_{zx} \\ \gamma_{xy} \end{Bmatrix} = \begin{Bmatrix} -1.43E-5 \\ -6.693E-3 \\ 0.011 \\ 4.676E-3 \\ 9.353E-3 \\ 3.118E-3 \end{Bmatrix}, \quad \begin{Bmatrix} \sigma_x \\ \sigma_y \\ \sigma_z \\ \tau_{yz} \\ \tau_{zx} \\ \tau_{xy} \end{Bmatrix} = \begin{Bmatrix} 9.789E+4 \\ 2.447E+4 \\ 2.203E+5 \\ 7.342E+4 \\ 1.468E+5 \\ 4.895E+4 \end{Bmatrix} \tag{21}
$$

The shear stresses on the 30 slip planes are calculated using Eqs. (15-16) as

$$
\begin{Bmatrix} \tau^1 \\ \tau^2 \\ \tau^3 \\ \tau^4 \\ \tau^5 \\ \tau^6 \\ \tau^7 \\ \tau^8 \\ \tau^9 \\ \tau^{10} \\ \tau^{11} \\ \tau^{12} \end{Bmatrix} = \begin{Bmatrix} -5.995E+4 \\ 1.199E+5 \\ 5.995E+5 \\ 3.996E+4 \\ -1.199E+5 \\ -1.599E+5 \\ -5.995E+4 \\ -3.996E+4 \\ -9.991E+4 \\ 0 \\ 0 \\ 0 \end{Bmatrix}, \quad \begin{Bmatrix} \tau^{13} \\ \tau^{14} \\ \tau^{15} \\ \tau^{16} \\ \tau^{17} \\ \tau^{18} \\ \tau^{19} \\ \tau^{20} \\ \tau^{21} \\ \tau^{22} \\ \tau^{23} \\ \tau^{24} \end{Bmatrix} = \begin{Bmatrix} -1.038E+5 \\ 0 \\ 1.038E+5 \\ -1.615E+5 \\ 1.154E+5 \\ 4.615E+4 \\ 8.076E+4 \\ -9.229E+4 \\ 1.154E+4 \\ 0 \\ 0 \end{Bmatrix}, \quad \begin{Bmatrix} \tau^{25} \\ \tau^{26} \\ \tau^{27} \\ \tau^{28} \\ \tau^{29} \\ \tau^{30} \end{Bmatrix} = \begin{Bmatrix} 1.384E+5 \\ -6.922E+4 \\ 8.652E+4 \\ -1.73E+4 \\ 1.557E+5 \\ -5.191E+4 \end{Bmatrix} \tag{22}
$$

The engineering shear strains on the 30 slip planes are

$$
\begin{Bmatrix} \gamma^1 \\ \gamma^2 \\ \gamma^3 \\ \gamma^4 \\ \gamma^5 \\ \gamma^6 \\ \gamma^7 \\ \gamma^8 \\ \gamma^9 \\ \gamma^{10} \\ \gamma^{11} \\ \gamma^{12} \end{Bmatrix} = \begin{Bmatrix} -9.725E-3 \\ 0.017 \\ 7.362E-3 \\ 8.452E-3 \\ -0.011 \\ -0.02 \\ -2.742E-4 \\ -0.012 \\ -0.012 \\ 9.451E-3 \\ 5.907E-3 \\ -3.544E-3 \end{Bmatrix}, \quad \begin{Bmatrix} \gamma^{13} \\ \gamma^{14} \\ \gamma^{15} \\ \gamma^{16} \\ \gamma^{17} \\ \gamma^{18} \\ \gamma^{19} \\ \gamma^{20} \\ \gamma^{21} \\ \gamma^{22} \\ \gamma^{23} \\ \gamma^{24} \end{Bmatrix} = \begin{Bmatrix} -0.014 \\ -1.364E-3 \\ 0.015 \\ -0.018 \\ 0.016 \\ 1.575E-3 \\ 0.014 \\ -7.243E-3 \\ -6.768E-3 \\ -1.364E-3 \\ -7.502E-3 \\ 8.867E-3 \end{Bmatrix}, \quad \begin{Bmatrix} \gamma^{25} \\ \gamma^{26} \\ \gamma^{27} \\ \gamma^{28} \\ \gamma^{29} \\ \gamma^{30} \end{Bmatrix} = \begin{Bmatrix} 8.818E-3 \\ -4.409E-3 \\ 5.511E-3 \\ -1.102E-3 \\ 9.92E-3 \\ -3.307E-3 \end{Bmatrix} \tag{23}
$$

The normal stresses and strains on the principal and secondary octahedral planes are

$$\begin{Bmatrix} \sigma_1^n \\ \sigma_2^n \\ \sigma_3^n \\ \sigma_4^n \end{Bmatrix} = \begin{Bmatrix} 293,700 \\ 130,500 \\ 32,630 \\ 0 \end{Bmatrix}, \quad \begin{Bmatrix} \varepsilon_1^n \\ \varepsilon_2^n \\ \varepsilon_3^n \\ \varepsilon_4^n \end{Bmatrix} = \begin{Bmatrix} 0.007185 \\ 0.001989 \\ -0.001128 \\ -0.002167 \end{Bmatrix} \qquad (24)$$

The normal stresses and strains on the cube slip planes are simply the normal stresses and strains in the material coordinate system along (100), (010), and (001) axes. This procedure is used to compute normal and shear stresses and strains in the material coordinate system, for uniaxial test specimens loaded in strain control, in different orientations.

Strain controlled LCF tests conducted at 1200 F in air for PWA1480/1493 uniaxial smooth specimens, for four different orientations, is shown in Table 3. The four specimen orientations are <001> (5 data points), <111> (7 data points), <213> (4 data points), and <011> (3 data points), for a total of 19 data points. Figure 5 shows the plot of strain range vs. Cycles to failure. A wide scatter is observed in the data with poor correlation for a power law fit. The first step towards applying the failure criteria discussed earlier is to compute the shear and normal stresses and strains on all the 30 slip systems, for each data point, for maximum and minimum test strain values, as outlined in the example problem. The maximum shear stress and strain for each data point, for min and max test strain values, is selected from the 30 values corresponding to the 30 slip systems. The maximum normal stress and strain value on the planes where the shear stress is maximum is also noted. These values are tabulated in Table 4. Both the maximum shear stress and maximum shear strain occur on the same slip system, for the 4 different configurations examined. For the <001> and <011> configurations the max shear stress and strain occur on the secondary slip system (τ^{14}, γ^{14} and τ^{15}, γ^{15} respectively). For the <111> and <213> configurations max shear stress and strain occur on the cube slip system (τ^{25}, γ^{25} and τ^{29}, γ^{29} respectively). Using Table 4 the composite failure parameters highlighted in Eqs. (1-4) can be calculated and plotted as a function of cycles to failure. In addition to the four failure parameters discussed, some other composite parameters are also plotted as a function of cycles to failure (N).

Figures (6-9) show that the four parameters based on polycrystalline fatigue failure parameters do not correlate well with the test data. The application of these parameters for single crystal material is somewhat different since they are evaluated on the slip systems that are thought to be the critical planes. The parameters that collapse the failure data well and give the best correlation with a power law fit are the maximum shear stress amplitude [$\Delta \tau_{max}$] shown in Fig. 10, the composite parameter [$(\Delta \tau_{max})(\Delta \gamma_{max} / 2)$] shown in Fig. 11, and the max principal shear stress amplitude (Tresca theory) shown in Fig. 13. The parameter $\Delta \tau_{max}$ is appealing to use for its simplicity, and its power law curve fit is shown in Eq. (25). It must be remembered that these curve fits are only valid for 1200F.

$$\Delta \tau_{max} = 397,758 \, N^{-0.1598} \qquad (25)$$

The correlation for $[\Delta \tau_{max}]$ would be better if some of the high stress data points are corrected for inelastic effects. Since the deformation mechanisms in single crystals are controlled by the propagation of dislocations driven by shear the $[\Delta \tau_{max}]$ might indeed be a good fatigue failure parameter to use. This parameter must be verified for a wider range of R-values and specimen orientations, and also at different temperatures and environmental conditions. Equation 25 will be used to calculate fatigue life at a critical blade tip location for the SSME turbine blade.

5.0   Application of Fatigue Failure Criteria to Finite Element Stress Analysis Results of Single Crystal Nickel Turbine Blades

Turbine blades used in the advanced high-pressure fuel turbopump (AHPFTP) are fabricated from single crystal nickel PWA1480/1493 material. Many of these blades have failed during operation due to the initiation and propagation of fatigue cracks from an area of high concentrated stress at the blade tip leading edge. Inspection of blades from other units in the test program revealed the presence of similar cracks in the turbine blades. During the course of the investigation an interesting development was brought to light. When the size of the fatigue cracks for the population of blades inspected was compared with the secondary crystallographic orientation β a definite relationship was apparent as shown in Fig. 14 [2, 14]. Secondary orientation does appear to have some influence over whether a crack will initiate and arrest or continue to grow until failure of the blade airfoil occurs. Figure 14 reveals that for β = 45+/- 15 deg tip cracks arrested after some growth or did not initiate at all. This suggests that perhaps there are preferential β orientations for which crack growth is minimized at the blade tip.

In an attempt to understand the effect of crystal orientation on blade stress response a three-dimensional FE model capable of accounting for primary and secondary crystal orientation variation was constructed. The Alternate High Pressure Fuel Turbo Pump (HPFTP/AT) first stage blade ANSYS finite element model (FEM) was cut from a large 3D cyclic symmetry model that includes the first and second stage blades and retainers, interstage spacer, disk and shaft, and the disk covers (Fig. 15). The blade dampers are represented with forces applied to the blade platforms at the damper contact locations. The models are geometrically nonlinear due to the contact surfaces between the separate components. The element type used for the blade material is the ANSYS SOLID45, an 8-noded 3D solid isoparametric element. Anisotropic material properties are allowed with this element type. ANSYS aligns the material coordinate system with the element coordinate system.

The effect of crystal orientation on blade stress response was studied by running 297 separate FE models to cover the complete range of primary and secondary crystal orientation variation. To generate the 297 material coordinate systems used for this study local coordinate systems were generated and the element coordinate systems aligned with them [15]. The material coordinate system is referenced to the blade casting coordinate system, shown if Fig. 16. The relative orientation of the primary axis of the material coordinate system to the casting coordinate system is shown in Fig. 17. Two angles, Δ and γ, locate the primary material axis relative to the casting axis, the third angle, β, is the clocking of the secondary material axis about the primary material axis. Figure 18 and Table 5 show the distribution of the 297 different material coordinate systems within the allowed 15 degree maximum deviation from the casting axis. The secondary repeats after 90 degrees, so only 0 to 80 degrees needs to be modeled.

The load conditions represent full power mainstage operation of the Space Shuttle Main Engine, referred to as 109% RPL SL (Rated Power Level Service Life). The shaft speed is 37,355 rpm, the airfoil temperature is approximately 1200 F, forces representing the blade damper radial sling load are applied to the blade platform, and aerodynamic pressure loads are applied to the blade surfaces and internal core.

Postprocessing of the 297 finite element results files presented a fairly difficult challenge, and represents a considerable amount of effort. Two FORTRAN programs were employed for the postprocessing work. The first selects the element results from the coded binary output files and places them into ASCII text files. The second program processes the ASCII files to calculate averaged nodal results, the resolved shear stresses and strains and the normal stresses and strains on the 30 slip systems, in the single crystal material coordinate system. It then calculates the parameters chosen for study and sorts them based on user set criteria.

The connection between the blade and disk are modeled with ANSYS COMBIN40 elements. These elements have one degree of freedom at each node. The nodal motion in that degree of freedom sets the separation or contact of these elements only. This element does not have the capability for friction tangent to the contact surface. For this model the nodal coordinate systems on the contacting surface of the blade firtree attachment were rotated so that one axis is normal to the surface. This is the degree of freedom used in the COMBIN40 element. The nodal coordinate systems on the disk contact surfaces were similarly oriented. An interesting feature of the ADAPCO model is that the blade is next to a cyclic symmetry section of the disk (a 1 of 50 piece) so that only the pressure side of the blade attachment contact surface nodes are nearly coincident to the disk. The suction side of the blade is clocked 7.2 degrees about the shaft from the mating surface on the disk. The blade and disk nodal coordinate systems for the suction side attachment are 7.2 degrees out of parallel to each other to account for this. Since the COMBIN40 element only acts on the one degree of freedom normal to the contact surfaces the 7.2 degree offset in physical location and orientation is properly accounted for. To run the blade model separate from the global model the nodal displacements of the disk nodes attached to the COMBIN40 elements were taken from a run of the global model and used as enforced displacements for what would become free ends of the contact elements.

Figure 19 shows representative Von Mises stress distribution plot for the turbine blade in the attachment region. The crack location and orientation at the critical blade tip location is shown in Fig. 14.

6 Effect of Secondary Crystal Orientation on Blade Tip Stress Response

Variation of secondary crystal orientation on stress response at the blade tip critical point prone to cracking (tip point on inside radius) was examined by analyzing the results from the 297 FE model runs. The FE node at the critical point was isolated and critical failure parameter value ($\Delta\tau_{max}$) computed on the 30 slip systems. A shaded contour plot of $\Delta\tau_{max}$ was generated as a function of primary and secondary orientation, shown in Fig. 20. The contour plot clearly shows a minimum value for $\Delta\tau_{max}$ for secondary orientation of β = 50 deg and primary orientation designated by cases 5 and 20. From Table 5.1 we see that case 5 corresponds to a primary orientation of Δ = 0 deg and γ = 7.5 deg. Case 20 corresponds to a primary orientation of Δ =

5.74 deg and γ = 13.86 deg. Using the fatigue life equation based on the $\Delta\tau_{max}$ curve fit of LCF test data, Eq. (25), we can obtain a contour plot of dimensionless life at the critical point as a function of primary and secondary orientation, as shown in Figure 21. The maximum life is again obtained for β = 50 deg, and Δ = 0 deg and γ = 7.5 deg, and Δ = 5.74 deg and γ = 13.86 deg. The optimum value of secondary orientation β = 50 deg. corresponds very closely to the optimum value of β indicated in Fig. 14. This demonstrates that control of secondary and primary crystallographic orientation has the potential to significantly increase a component's resistance to fatigue crack growth without adding additional weight or cost.

7.0 CONCLUSIONS

Fatigue failure in PWA1480/1493, a single crystal nickel base turbine blade superalloy, is investigated using a combination of experimental LCF fatigue data and 3D FE modeling of HPFTP/AT SSME turbine blades. Several failure criteria, based on the normal and shear stresses and strains on the 24 octahedral and 6 cube slip systems for a FCC crystal, are evaluated for strain controlled uniaxial LCF data (1200 F in air). The maximum shear stress amplitude [$\Delta\tau_{max}$] on the 30 slip systems was found to be an effective fatigue failure criterion, based on the curve fit between $\Delta\tau_{max}$ and cycles to failure. Since deformation mechanisms in single crystals are controlled by the propagation of dislocations driven by shear, $\Delta\tau_{max}$ might indeed be a good fatigue failure parameter to use. However, this parameter must be verified for a wider range of R-values and specimen orientations, and also at different temperatures and environmental conditions.

Investigation of leading edge tip cracks in operational SSME turbine blades had revealed that secondary crystal orientation appeared to influence whether a crack initiated and arrested or continued to grow until failure of the blade airfoil. The turbine blade was modeled using 3D FEA that is capable of accounting for material orthotrophy and variation in primary and secondary crystal orientation. Effects of variation in crystal orientation on blade stress response were studied based on 297 FE model runs. Fatigue life at the critical locations in blade was computed using FE stress results and failure criterion developed. Detailed analysis of the results revealed that secondary crystal orientation had a pronounced effect on fatigue life. The optimum value of secondary orientation β = 50° computed corresponds very closely to the optimum value of β indicated in the failed population of blades. Control of secondary and primary crystallographic orientation has the potential to significantly increase a component's resistance to fatigue crack growth without adding additional weight or cost.

8.0 References

1.   Cowles, B. A., "High cycle fatigue failure in aircraft gas turbines: An industry perspective," *International Journal of Fracture*, Vol. 80, pp. 147-163, 1996.

2.   Moroso, J, "Effect of secondary crystal orientation on fatigue crack growth in single crystal nickel turbine blade superalloys," *M. S. Thesis*, Mechanical Engineering Department, University of Florida, Gainesville, FL, May 1999.

3.   Deluca, D., Annis, C.; "Fatigue in Single Crystal Nickel Superalloys"; Office of Naval
      Research, Department of the Navy FR23800, August 1995

4.   Stouffer, D. C., and Dame, L. T., "Inelastic Deformation of Metals," John Wiley & Sons,
      1996.

5.   Milligan, W. W., and Antolovich, S. D., "Deformation modeling and constitutive
      modeling for anisotropic superalloys," NASA Contractor Report 4215, February 1985.

6.   Telesman, J.; Ghosn, L, "The unusual near threshold FCG behavior of a single crystal
      superalloy and the resolved shear stress as the crack driving force," *Engineering Fracture
      Mechanics*, Vol. 34, No. 5/6, pp. 1183-1196, 1989.

7.   Deluca, D. P. and Cowles, B. A., "Fatigue and fracture of single crystal nickel in high
      pressure hydrogen", *Hydrogen Effects on Material Behavior*, Ed. By N. R. Moody and A.
      W. Thomson, TMS., Warrendale, PA, 1989..

8.   Kandil, F. A., Brown, M. W., and Miller, K. J., "Biaxial low cycle fatigue of 316
      stainless steel at elevated temperatures," Book, pp. 203-210, Metals Soc., London, 1982.

9.   Socie, D. F., Kurath, P., and Koch,J., "A multiaxial fatigue damage parameter," presented
      at the Second International Symposium on Multiaxial Fatigue, Sheffield, U.K., 1985.

10.   Fatemi, A, Socie, D, "A Critical Plane Approach to Multiaxial Fatigue Damage Including
      Out-of-Phase Loading," *Fatigue Fracture in Engineering Materials*, Vol. 11, No. 3, pp.
      149-165, 1988.

11.   Smith, K. N., Watson, P., and Topper, T. M., "A stress-strain function for the fatigue of
      metals," *Journal of Materials*, Vol. 5, No. 4, pp. 767-778, 1970.

12.   Banantine, J. A., and socie, D. F., "Observations of cracking behavior in tension and
      torsion low cycle fatigue," presented at ASTM Symposium on low cycle fatigue –
      Directions for the future, Philadelphia, 1985.

13.   Lekhnitskii, S. G., "Theory of elasticity of an anisotropic elastic body," Book, pp. 1-40,
      Holden-Day Inc. Publishers, 1963.

14.   Pratt and Whitney, "SSME Alternate Turbopump Development Program HPFTP Critical
      Design Review," P&W FR24581-1 December 23, 1996. NASA Contract NAS8-36801.

15.   Sayyah, T., "Alternate Turbopump Development Single Crystal Failure Criterion for
      High Pressure Fuel Turbopump First Stage Blades," Report No.: 621-025-99-001, NASA
      Contract NAS 8-40836, May 27, 1999.

	x	y	z
x'	α_1	β_1	γ_1
y'	α_2	β_2	γ_2
z'	α_3	β_3	γ_3

Table 1 Direction Cosines

	x	y	z
x'	$\alpha_1=0.5445$	$\beta_1=0.2673$	$\gamma_1=0.8018$
y'	$\alpha_2=-0.8320$	$\beta_2=0.0$	$\gamma_2=0.5547$
z'	$\alpha_3=0.1482$	$\beta_3=-0.9636$	$\gamma_3=0.2223$

Table 2 Direction Cosines

Specimen Orientation	Max Test Strain	Min Test Strain	R Ratio	Strain Range	Cycles to Failure
<001>	.01509	.00014	0.01	.01495	1326
<001>	.0174	.0027	0.16	0.0147	1593
<001>	.0112	.0002	0.02	0.011	4414
<001>	.01202	.00008	0.01	0.0119	5673
<001>	.00891	.00018	0.02	.00873	29516
<111>	.01219	-0.006	-0.49	.01819	26
<111>	.0096	.0015	0.16	0.0081	843
<111>	.00809	.00008	0.01	.00801	1016
<111>	.006	0.0	0.0	0.006	3410
<111>	.00291	-0.00284	-0.98	.00575	7101
<111>	.00591	.00015	0.03	.00576	7356
<111>	.01205	0.00625	0.52	0.0058	7904
<213>	.01212	0.0	0.0	.01212	79
<213>	.00795	.00013	0.02	.00782	4175
<213>	.00601	.00005	0.01	.00596	34676
<213>	.006	0.0	0.0	0.006	114789
<011>	.0092	.0004	0.04	0.0088	2672
<011>	.00896	.00013	0.01	.00883	7532
<011>	.00695	.00019	0.03	.00676	30220

Table 3 Strain controlled LCF test data for PWA1493 at 1200 F for 4 specimen orientations

γ_{max} = Max shear strain of 30 slip systems for max specimen test strain value
γ_{min} = Max shear strain of 30 slip systems for min specimen test strain value
τ_{max} = Max shear stress of 30 slip systems for max specimen test strain value
τ_{min} = Max shear stress of 30 slip systems for min specimen test strain value

Specimen Orientation	γ_{max}	γ_{min}	$\Delta\gamma/2$	ε_{max}	ε_{min}	$\Delta\varepsilon/2$	τ_{max} psi	τ_{min} psi	$\Delta\tau$ psi	σ_{max} psi	σ_{min} psi	$\Delta\sigma$ psi	Cycles to Failure
<001> $\tau_{max} = \tau^{14}$ $\gamma_{max} = \gamma^{14}$	0.02	0.000185	0.0099075	0.00097	9.25E-06	0.0004804	1.10E+05	1016	1.08E+05	7.75E+04	719	7.68E+04	1326
	0.023	0.0036	0.0097	0.0015	1.78E-04	0.000661	1.26E+05	1.96E+04	1.06E+05	8.93E+04	1.39E+04	7.54E+04	1593
	0.015	2.64E-04	0.007368	7.34E-04	1.32E-05	0.0003604	8.13E+04	1452	7.98E+04	5.75E+04	1027	5.65E+04	4414
	0.016	0	0.008	7.94E-04	0	0.000397	8.73E+04	0	8.73E+04	6.17E+04	0	6.17E+04	5673
	0.012	0	0.006	5.89E-04	0	0.0002945	6.47E+04	0	6.47E+04	4.57E+04	0	4.57E+04	29516
<111> $\tau_{max} = \tau^{25}$ $\gamma_{max} = \gamma^{25}$	0.014	-7.06E-03	0.01053	2.05E-03	-1.01E-03	0.00153	2.25E+05	-1.10E+05	3.35E+05	1.59E+05	-7.80E+04	2.37E+05	26
	0.011	0.00176	0.00462	0.0016	0.00025	0.000675	1.77E+05	2.77E+04	1.49E+05	1.25E+05	1.96E+04	1.05E+05	843
	.0095	9.40E-05	0.004703	0.00136	1.34E-05	0.0006733	1.49E+05	1478	1.48E+05	1.06E+05	1045	1.05E+05	1016
	.0076	0	0.0038	0.001	0	0.0005	1.10E+05	0	1.10E+05	7.84E+04	0	7.84E+04	3410
	.0034	-0.0033	0.00335	0.00049	-0.00048	0.000485	5.40E+04	-5.30E+04	1.07E+05	3.80E+04	-3.70E+04	7.50E+04	7101
	.0069	1.76E-04	0.003362	9.90E-04	2.50E-05	0.0004825	1.09E+05	2771	1.06E+05	7.70E+04	1959	7.50E+04	7356
	0.014	0.007	0.0035	0.002	0.001	0.0005	2.25E+05	1.10E+05	1.15E+05	1.60E+05	7.80E+04	8.20E+04	7904
<213> $\tau_{max} = \tau^{29}$ $\gamma_{max} = \gamma^{29}$	0.018	0	0.009	0.002	0	0.001	1.60E+05	0	1.60E+05	1.30E+05	0	1.30E+05	79
	0.012	1.90E-04	0.005905	0.0013	2.10E-05	0.0006395	1.06E+05	1732	1.04E+05	8.60E+04	1400	8.46E+04	4175
	.0088	0	0.0044	0.00098	0	0.00049	8.00E+04	0	8.00E+04	6.50E+04	0	6.50E+04	34676
	.0088	0	0.0044	0.00098	0	0.00049	8.00E+04	0	8.00E+04	6.50E+04	0	6.50E+04	114789
<011> $\tau_{max} = \tau^{15}$ $\gamma_{max} = \gamma^{15}$	0.015	6.50E-04	0.007175	0.0039	1.68E-04	0.001866	1.23E+05	5333	1.18E+05	1.73E+05	7538	1.65E+05	2672
	0.015	0	0.0075	0.0039	0	0.00195	1.23E+05	0	1.23E+05	1.70E+05	0	1.70E+05	7532
	0.011	3.10E-04	0.005345	0.0029	8.00E-05	0.00141	9.30E+04	2532	9.05E+04	1.31E+05	3581	1.27E+05	30220

Table 4 Maximum values of shear stress and shear strain on the slip systems and normal stress and strain values on the same planes.

Case	Delta	Gamma	Beta
0	0.00	0.00	0,10,20,30,40,50,60,70,80
1	7.50	0.00	0,10,20,30,40,50,60,70,80
2	6.93	2.87	0,10,20,30,40,50,60,70,80
3	5.30	5.30	0,10,20,30,40,50,60,70,80
4	2.87	6.93	0,10,20,30,40,50,60,70,80
5	0.00	7.50	0,10,20,30,40,50,60,70,80
6	-2.87	6.93	0,10,20,30,40,50,60,70,80
7	-5.30	5.30	0,10,20,30,40,50,60,70,80
8	-6.93	2.87	0,10,20,30,40,50,60,70,80
9	-7.50	0.00	0,10,20,30,40,50,60,70,80
10	-6.93	-2.87	0,10,20,30,40,50,60,70,80
11	-5.30	-5.30	0,10,20,30,40,50,60,70,80
12	-2.87	-6.93	0,10,20,30,40,50,60,70,80
13	0.00	-7.50	0,10,20,30,40,50,60,70,80
14	2.87	-6.93	0,10,20,30,40,50,60,70,80
15	5.30	-5.30	0,10,20,30,40,50,60,70,80
16	6.93	-2.87	0,10,20,30,40,50,60,70,80
17	15.00	0.00	0,10,20,30,40,50,60,70,80
18	13.86	5.74	0,10,20,30,40,50,60,70,80
19	10.61	10.61	0,10,20,30,40,50,60,70,80
20	5.74	13.86	0,10,20,30,40,50,60,70,80
21	0.00	15.00	0,10,20,30,40,50,60,70,80
22	-5.74	13.86	0,10,20,30,40,50,60,70,80
23	-10.61	10.61	0,10,20,30,40,50,60,70,80
24	-13.86	5.74	0,10,20,30,40,50,60,70,80
25	-15.00	0.00	0,10,20,30,40,50,60,70,80
26	-13.86	-5.74	0,10,20,30,40,50,60,70,80
27	-10.61	-10.61	0,10,20,30,40,50,60,70,80
28	-5.74	-13.86	0,10,20,30,40,50,60,70,80
29	0.00	-15.00	0,10,20,30,40,50,60,70,80
30	5.74	-13.86	0,10,20,30,40,50,60,70,80
31	10.61	-10.61	0,10,20,30,40,50,60,70,80
32	13.86	-5.74	0,10,20,30,40,50,60,70,80

Table 5 33 primary axis cases with 9 secondary cases each, for a total of 297 material orientations.
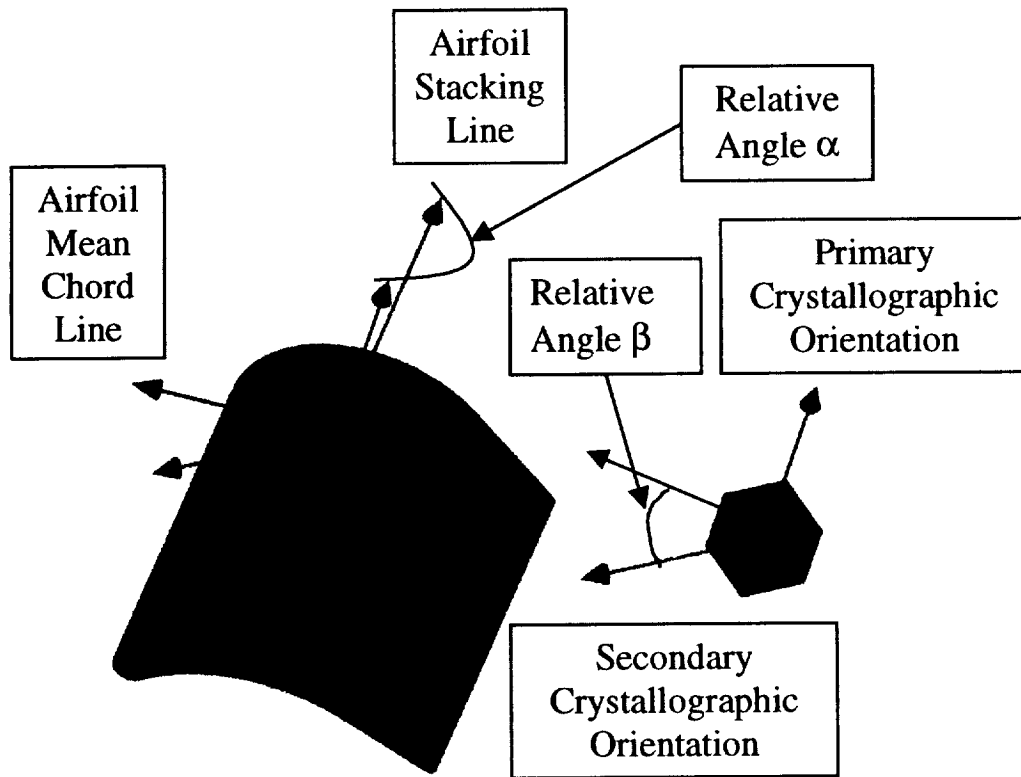
Fig. 1 Convention for Defining Crystal Orientation in Turbine Blades[2]
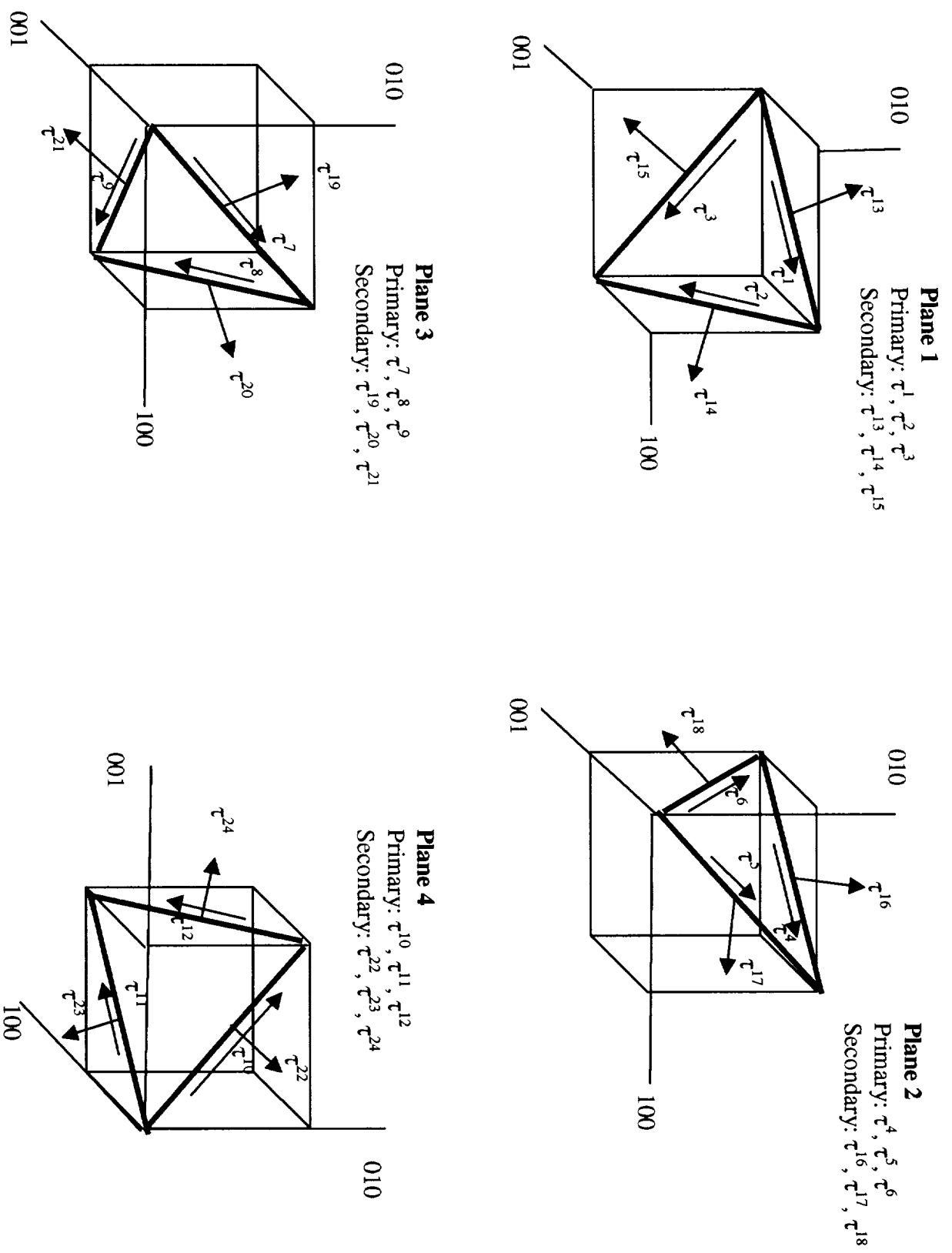
Fig. 2 Primary (close-pack) and secondary (non-close-pack) slip directions on the octahedral planes for a FCC crystal [4]

Plane 1
Primary: τ^1, τ^2, τ^3
Secondary: $\tau^{13}, \tau^{14}, \tau^{15}$

Plane 2
Primary: τ^4, τ^5, τ^6
Secondary: $\tau^{16}, \tau^{17}, \tau^{18}$

Plane 3
Primary: τ^7, τ^8, τ^9
Secondary: $\tau^{19}, \tau^{20}, \tau^{21}$

Plane 4
Primary: $\tau^{10}, \tau^{11}, \tau^{12}$
Secondary: $\tau^{22}, \tau^{23}, \tau^{24}$
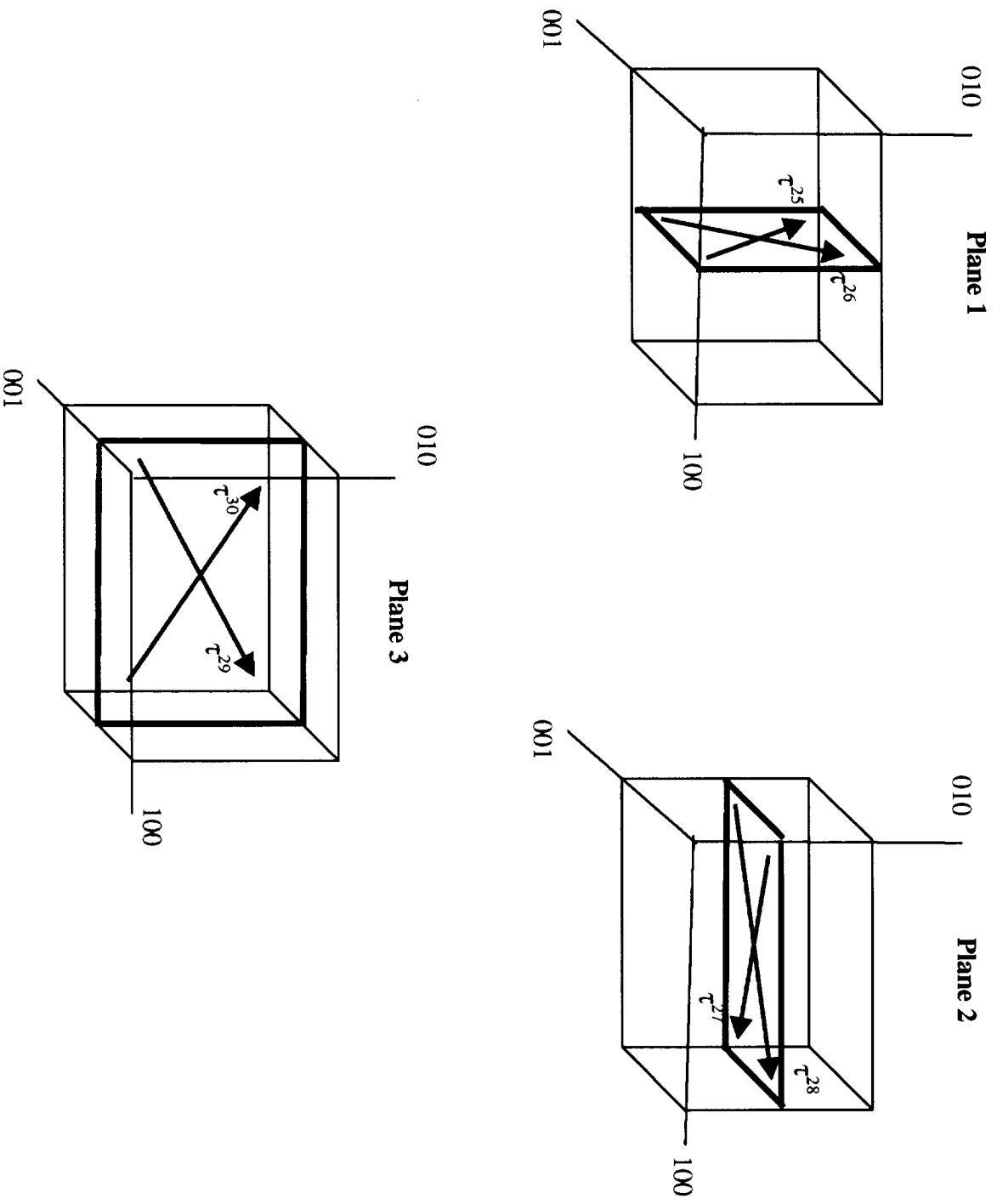
Fig. 3 Cube slip planes and slip directions for a FCC crystal [4]
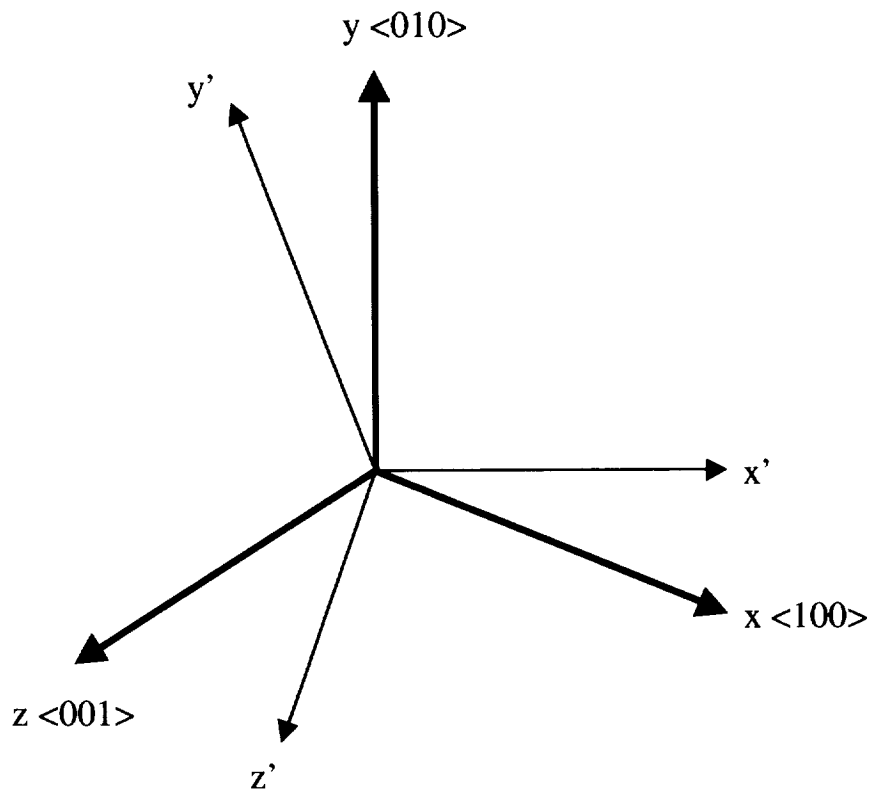
Figure 4 Material (x, y, z) and specimen (x', y', z') coordinate systems
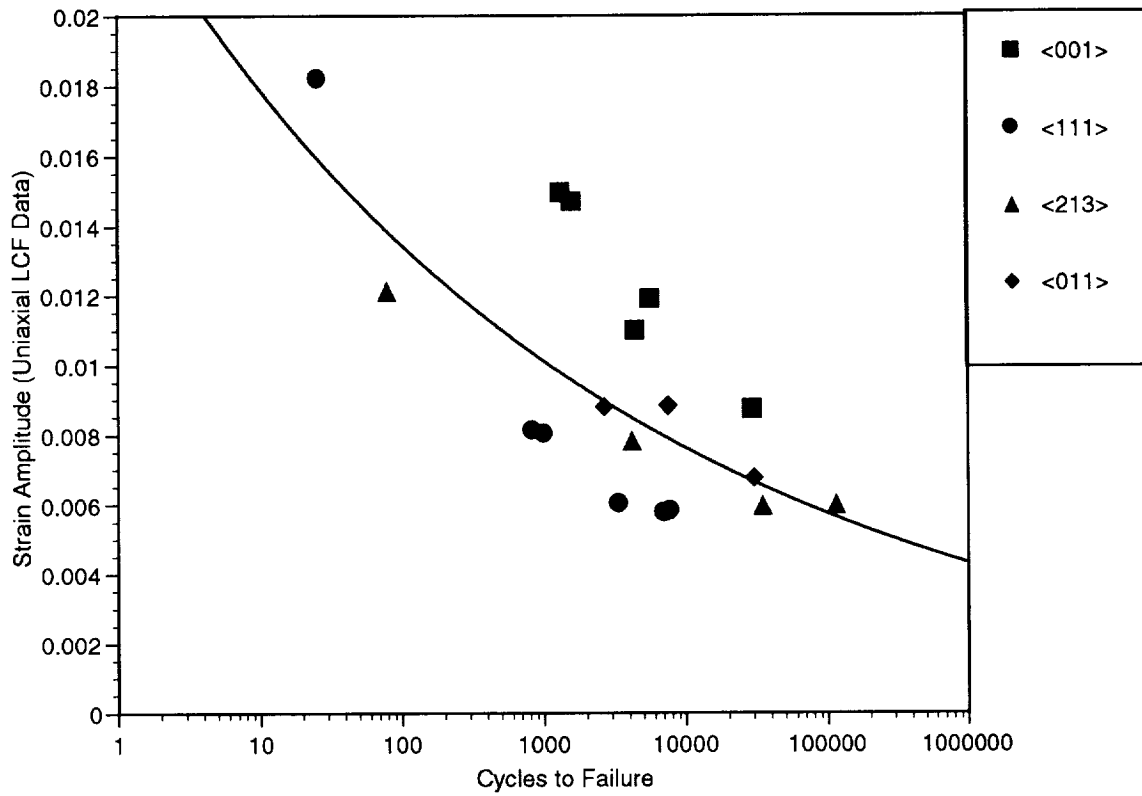
Fig. 5 Strain range Vs. Cycles to Failure for LCF test data (PWA1493 at 1200F)

Power Law Curve Fit (R^2 = 0.130): $[\gamma_{max} + \varepsilon_n] = 0.0249\ N^{-0.773}$
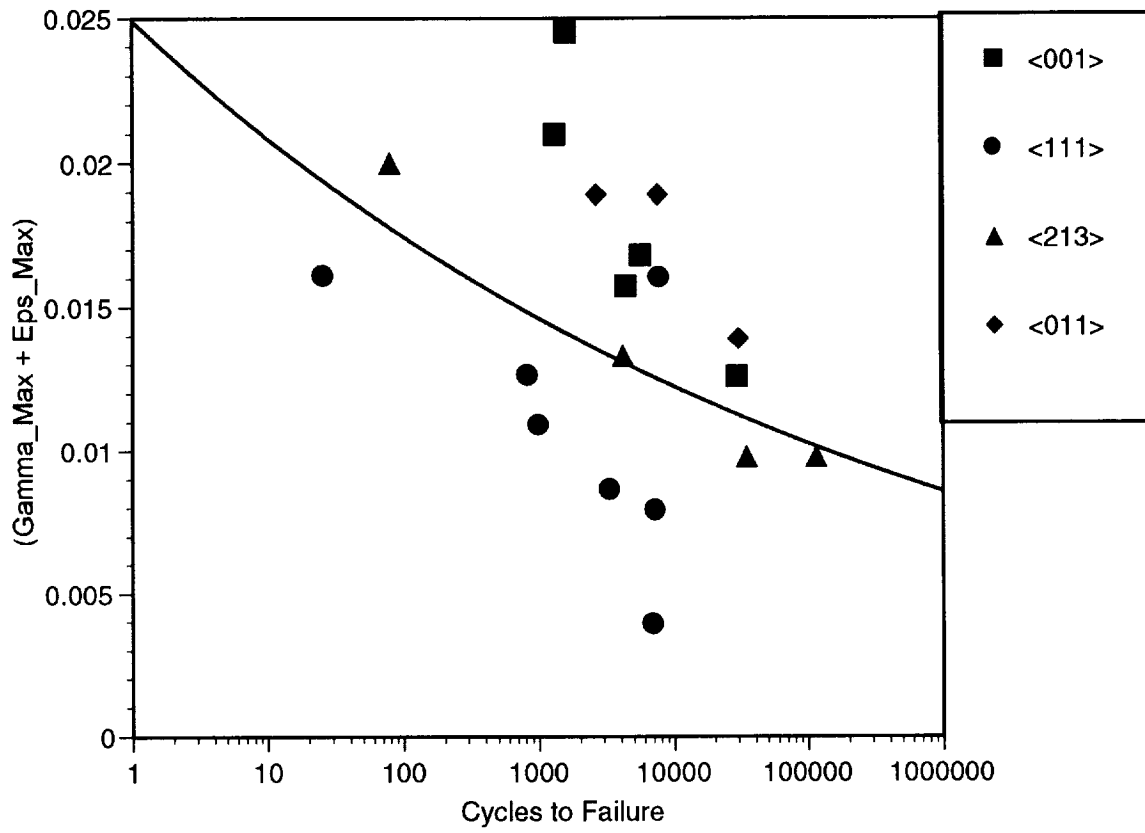
Fig. 6 $[\gamma_{max} + \varepsilon_n]$ (Eq. 1) Vs. N

Power Law Curve Fit (R^2 = 0.391): $\left[\dfrac{\Delta\gamma}{2}+\dfrac{\Delta\varepsilon_n}{2}+\dfrac{\sigma_{no}}{E}\right] = 0.0206\ N^{-0.101}$
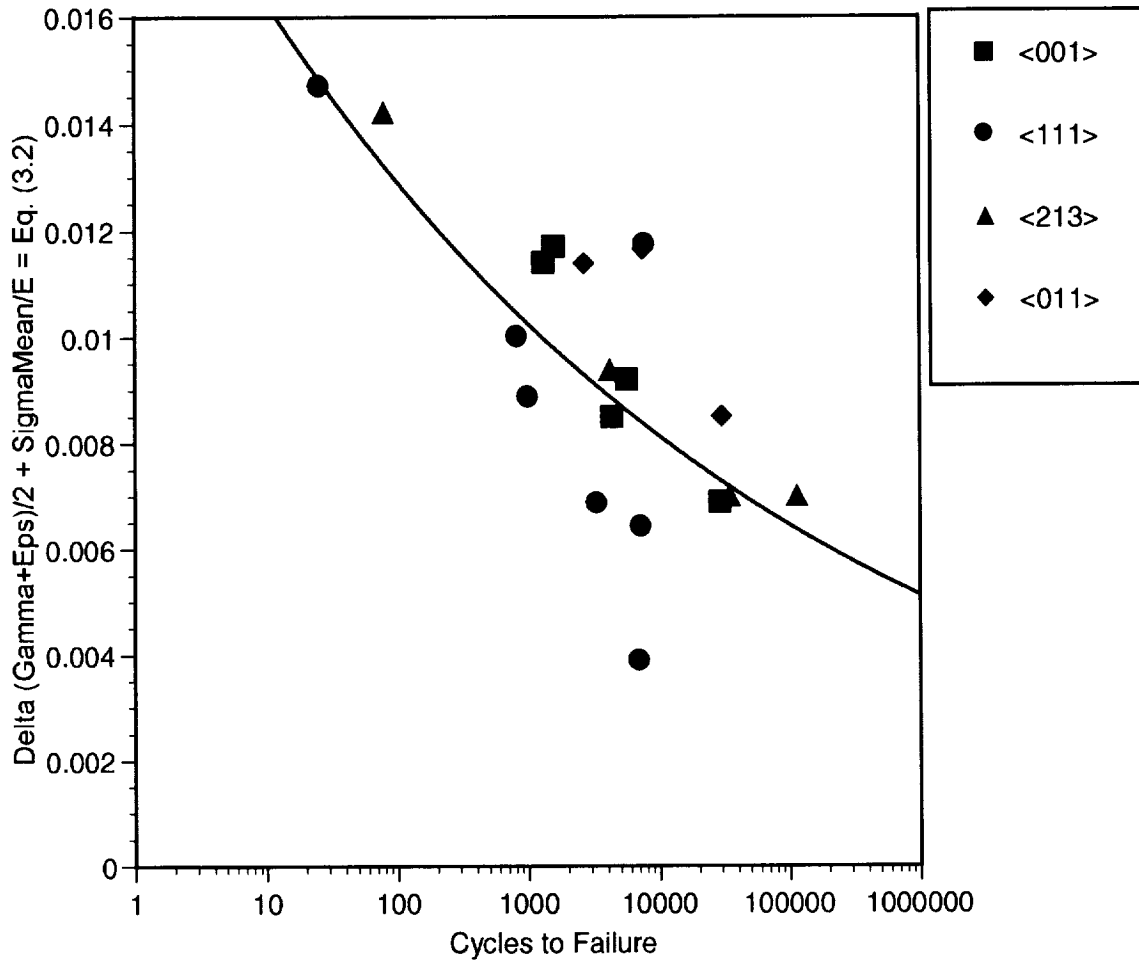
Fig. 7 $\left[\dfrac{\Delta\gamma}{2}+\dfrac{\Delta\varepsilon_n}{2}+\dfrac{\sigma_{no}}{E}\right]$ (Eq. 2) Vs. N

Power Law Curve Fit (R^2 = 0.383): $\left[\dfrac{\Delta\gamma}{2}(1+k\dfrac{\sigma_n^{max}}{\sigma_y}) \right] = 0.0342 \, N^{-0.143}$
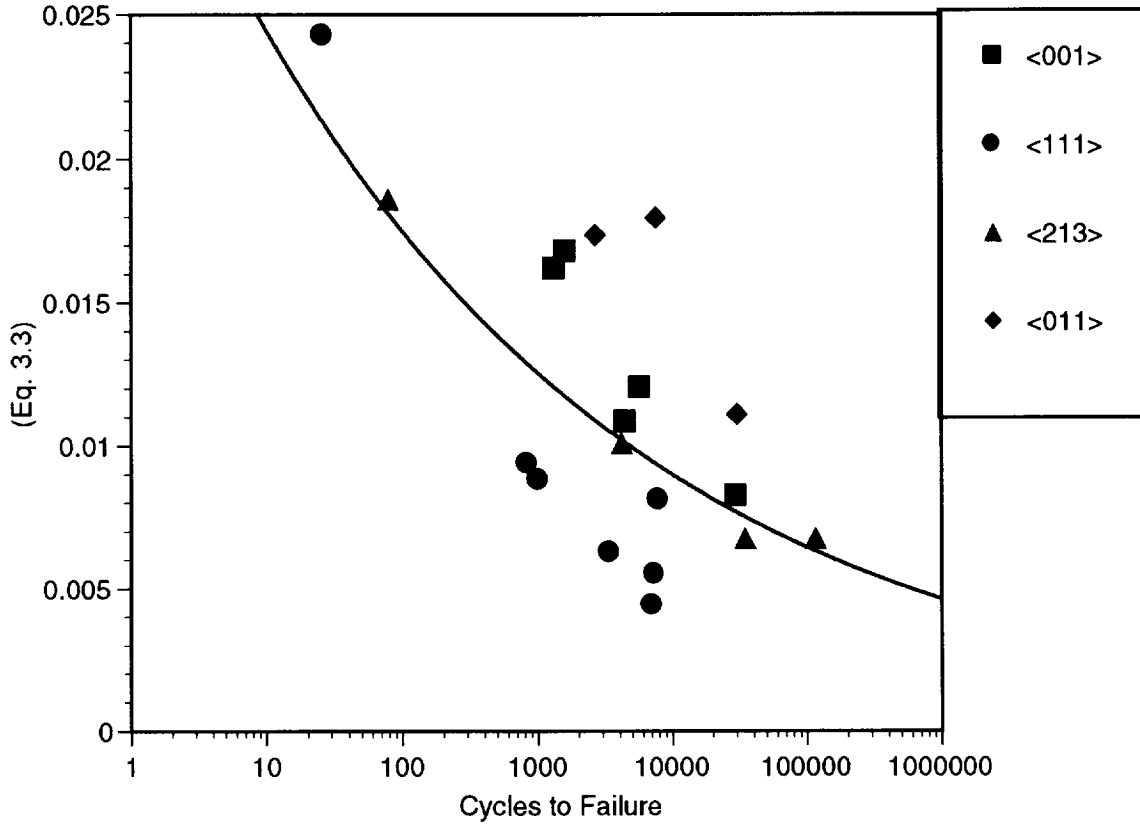
Fig. 8 $\left[\dfrac{\Delta\gamma}{2}(1+k\dfrac{\sigma_n^{max}}{\sigma_y}) \right]$ (Eq. 3) Vs. N

Power Law Curve Fit (R^2 = 0.189): $\left[\dfrac{\Delta \varepsilon_1}{2} (\sigma^{max}) \right] = 334.6 \, N^{-0.209}$

Fig. 4.7 $\left[\dfrac{\Delta \varepsilon_1}{2} (\sigma^{max}) \right]$ (Eq. 4) Vs. N
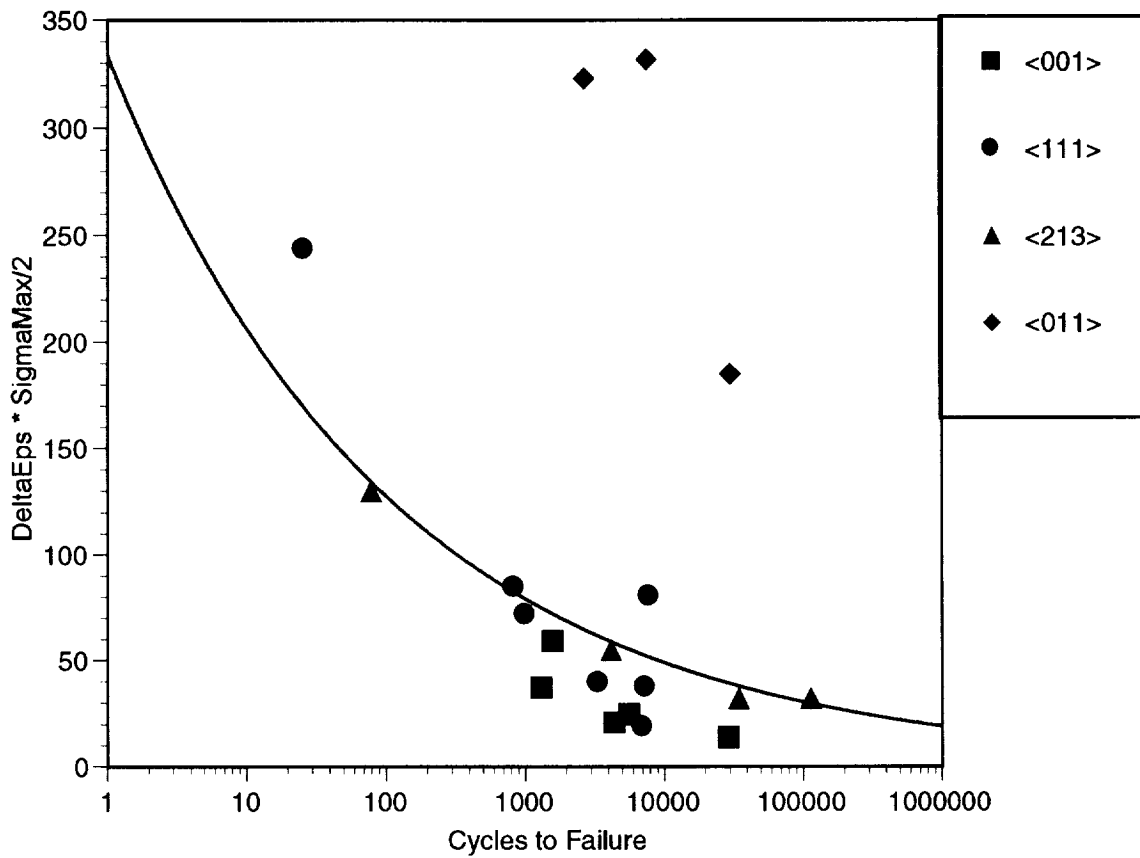
Power Law Curve Fit (R^2 = 0.674): $\Delta\tau = 397{,}758\ N^{-0.1598}$
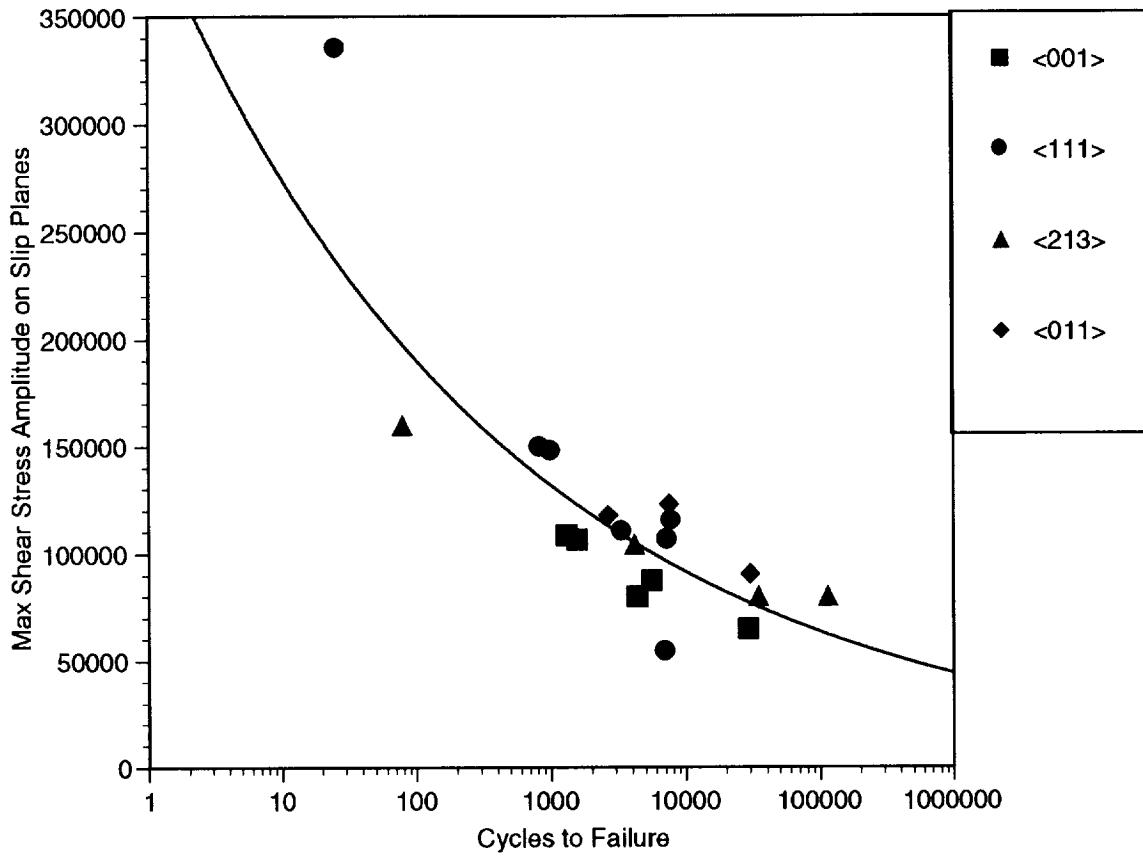
Fig. 10 Shear Stress Amplitude [$\Delta\tau_{max}$] Vs. N

Power Law Curve Fit (R^2 = 0.744): $\Delta\tau_{max} * \Delta\gamma/2 = 2{,}641\ N^{-0.256}$

Fig. 11 $\left[\Delta\tau_{max}\ \dfrac{\Delta\gamma_{max}}{2}\right]$ Vs. N
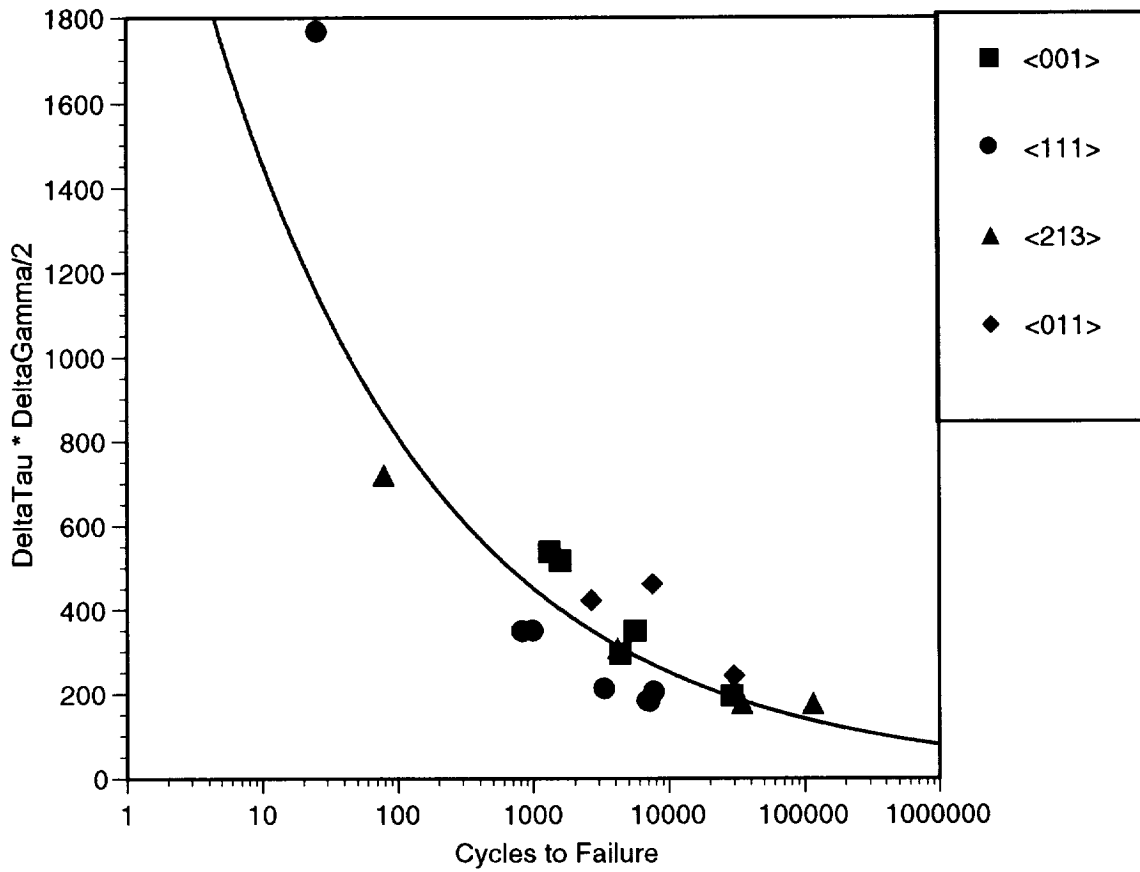
Power Law Curve Fit (R^2 = 0.549): $\tau_{max} * \Delta\gamma/2 = 4{,}661\ N^{-0.227}$

Fig. 12 $\left[\tau_{max} \dfrac{\Delta\gamma_{max}}{2} \right]$ Vs. N
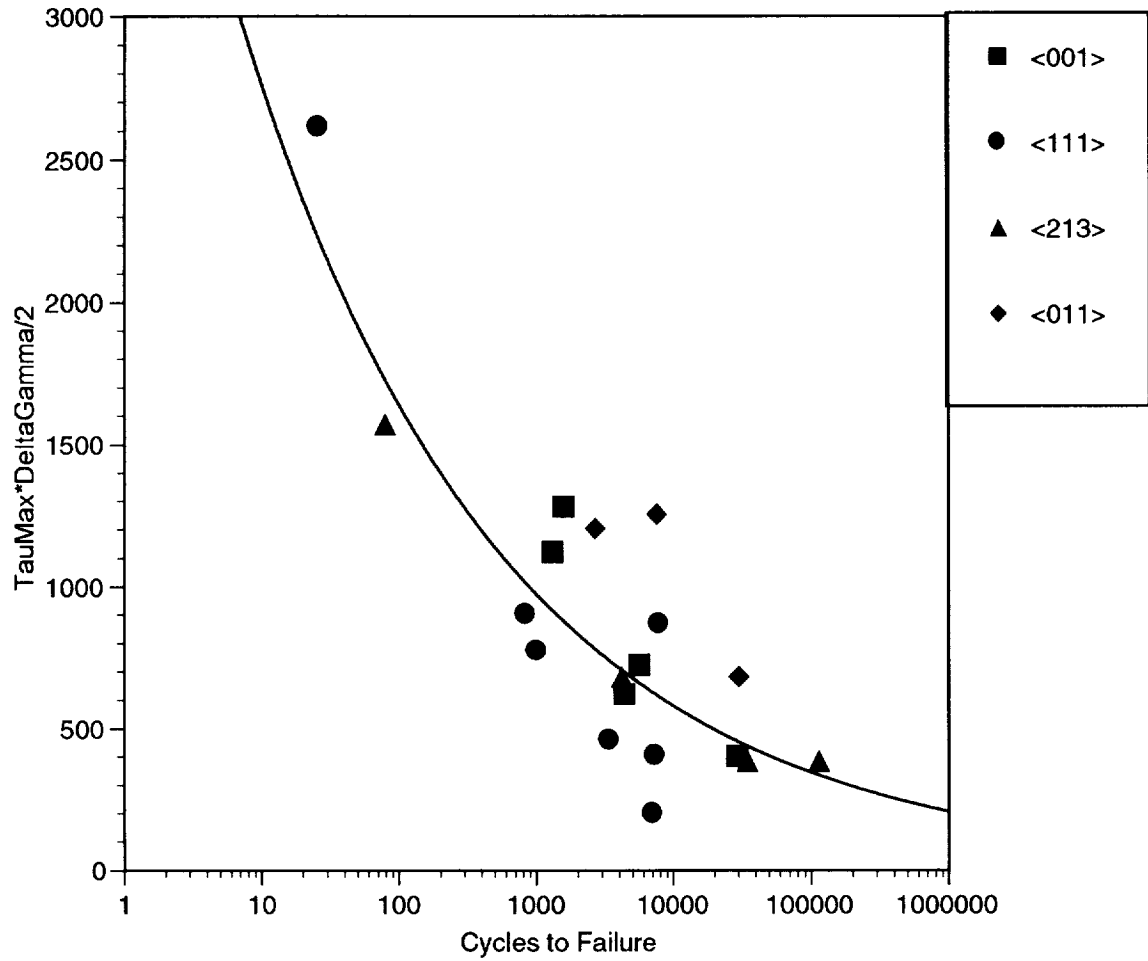
Power Law Curve Fit (R^2 = 0.775): $\Delta\tau_{Tresca} = 422{,}946\ N^{-0.157}$
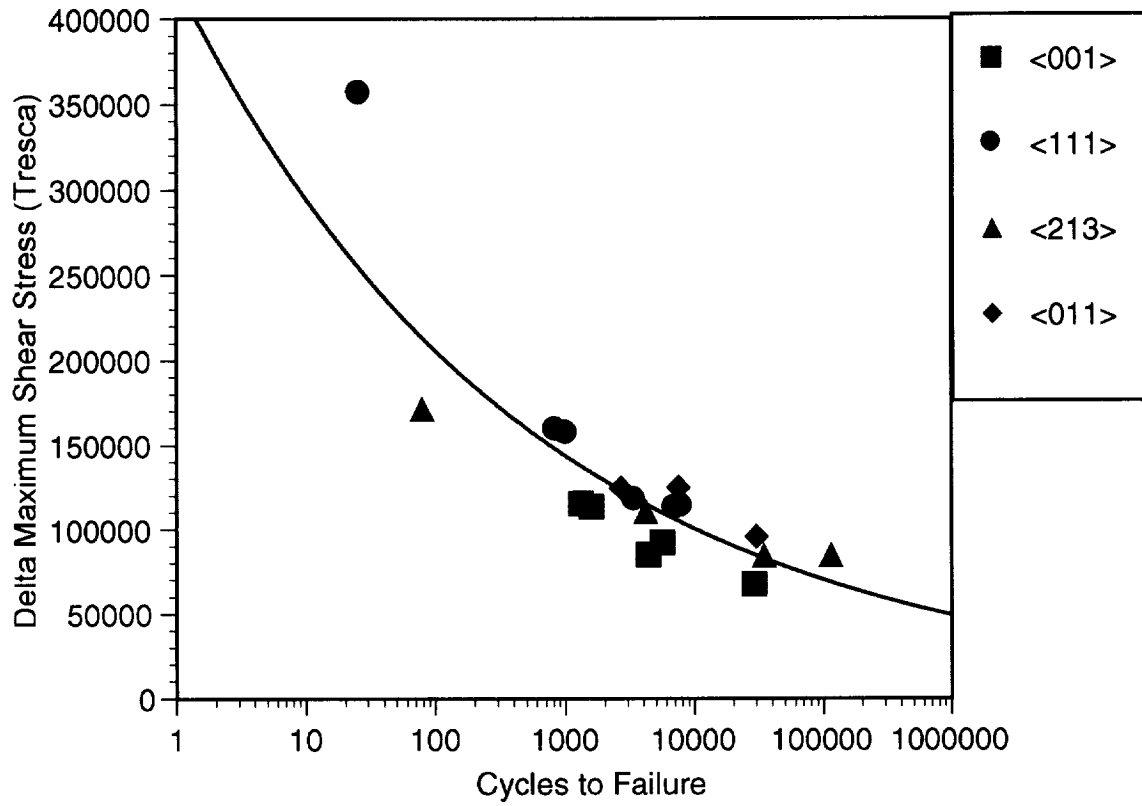
Fig. 13 $\Delta\tau_{Tresca}$ Vs. N
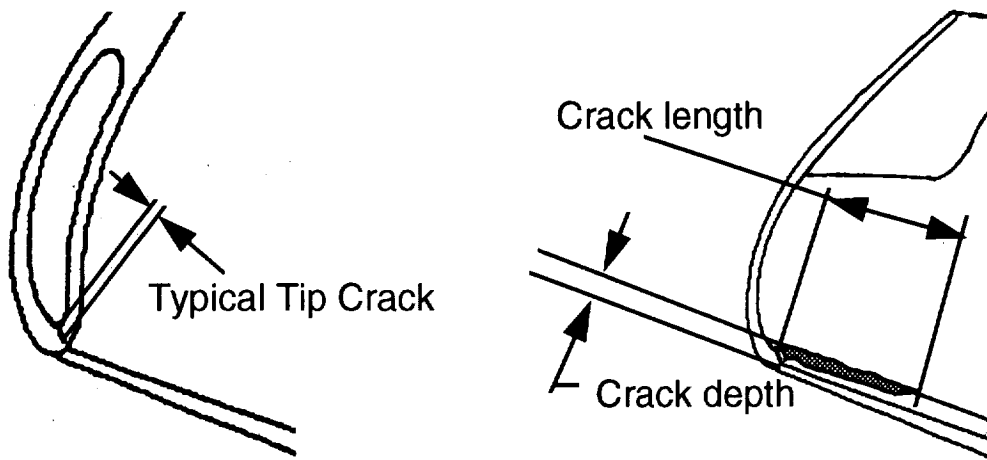
Blade leading edge crack location and orientation
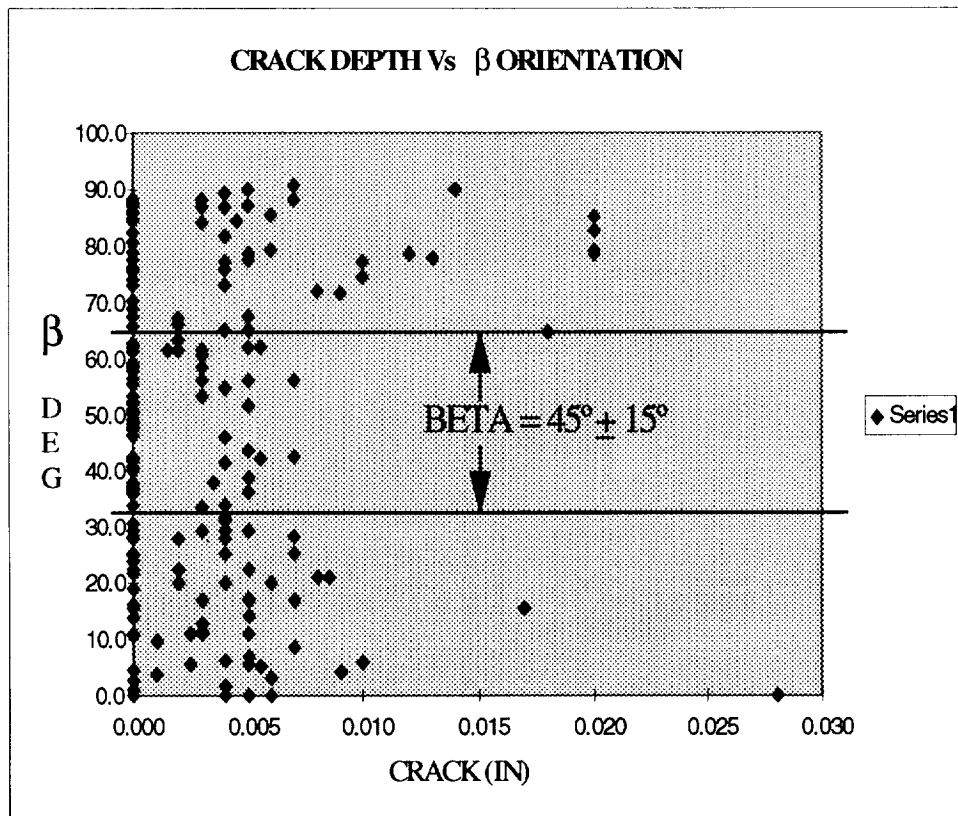
Figure 14 Secondary Crystallographic Orientation, β, Vs Crack Depth for the SSME
AHPFTP 1st Stage Turbine Blade[2]

$\Delta T / h r \epsilon \dot{\tau} \rho$
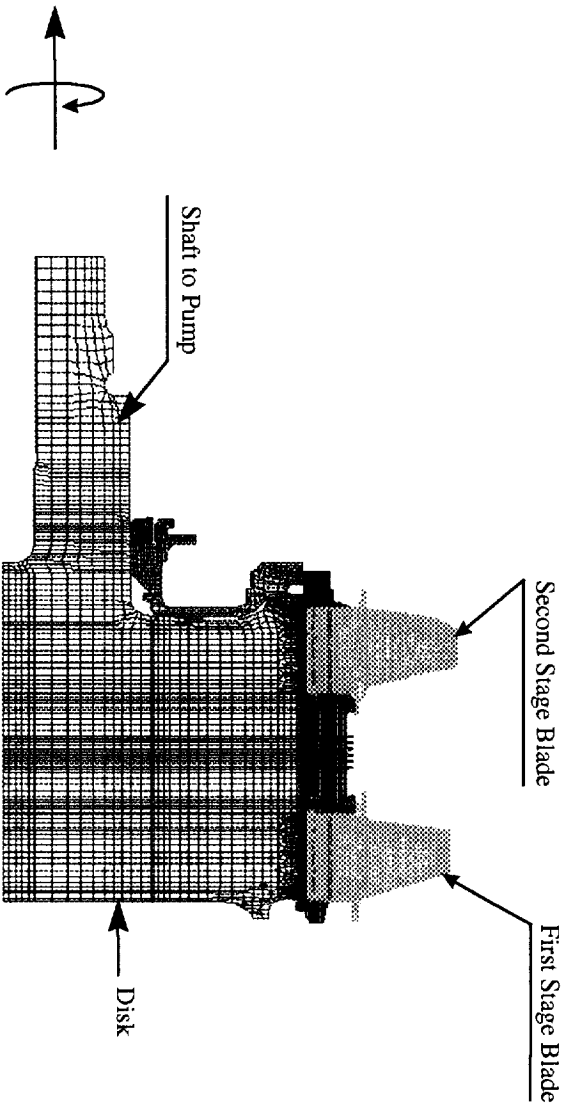
Figure 15 Three-Dimensional ANSYS model of HPFTP/AT rotating turbine

The Blade Leading
Edge

Top View of the Blade

Casting X
(γ → Axis

15 degrees (Limit of acceptable
primary axis per
Pratt & Whitney

(Δ) Casting Y
Axis
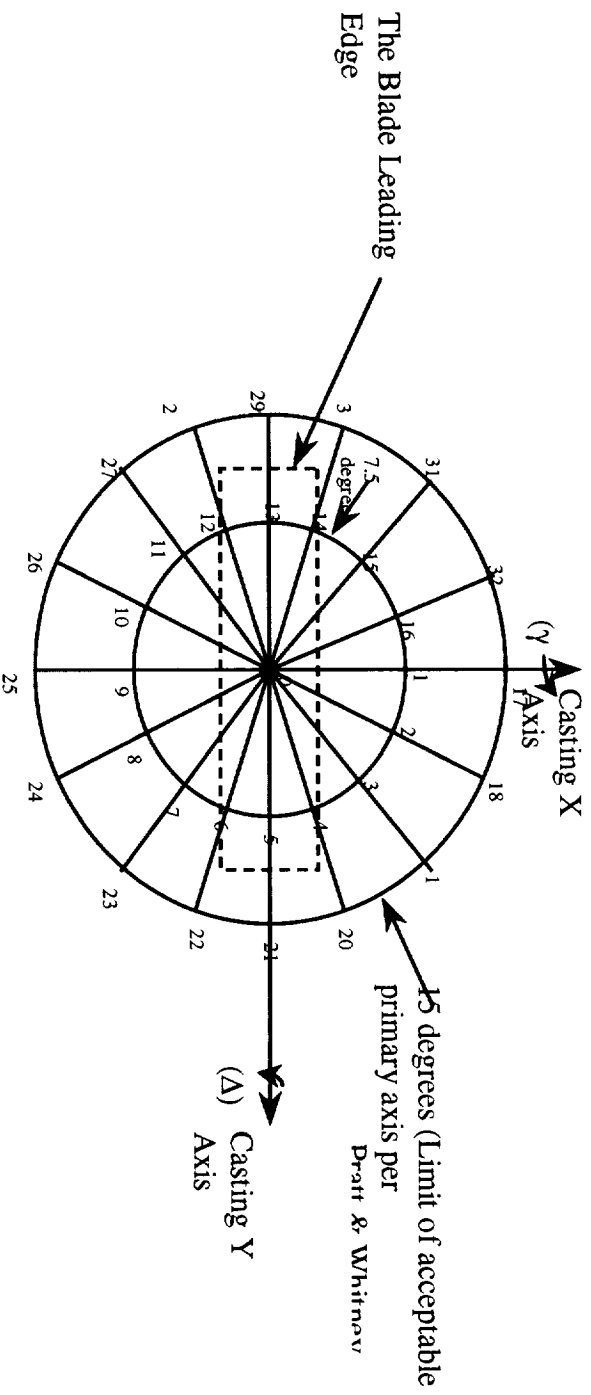
* (33) orientations (cases) of (γ & Δ) with (9) (θ)orientations about each of these.
  * 16 cases with (γ & Δ) combined to 7.5 degrees, 16 with (γ & Δ) combined to 15 degrees, 1 case
    with (γ & Δ) combined to 0 degrees.
  * (θ) varied from 0 to 80 degrees in 10 degree increments about the local material axis (due to
    symmetry 90 degrees is the same as 0 degree).
* Total of (297) orientations.

Figure 18 33 primary axis cases with 9 secondary cases each, for a total of 297 material orientations.
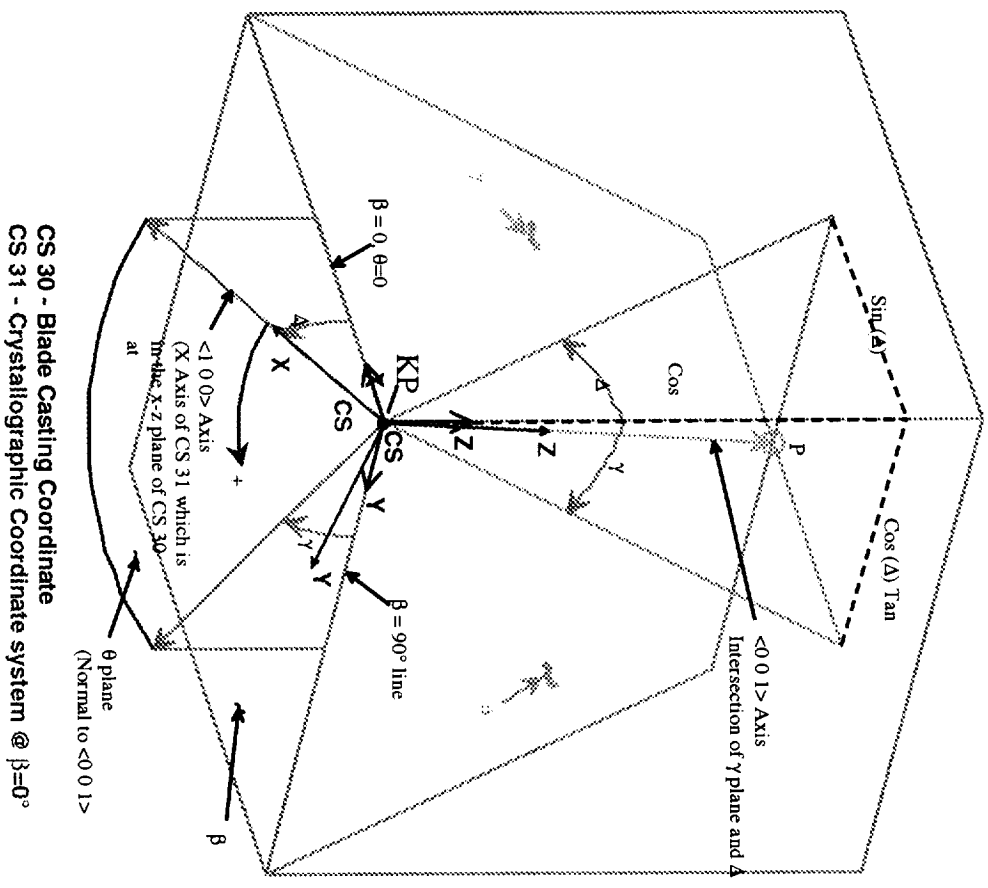
Figure 17 First stage blade material coordinate system relative to the casting coordinate

First Stage Blade Casting Coordinate System (CS 30)
Z axis along stacking axis pointing radially inward.
X axis pointing away from the pressure side.
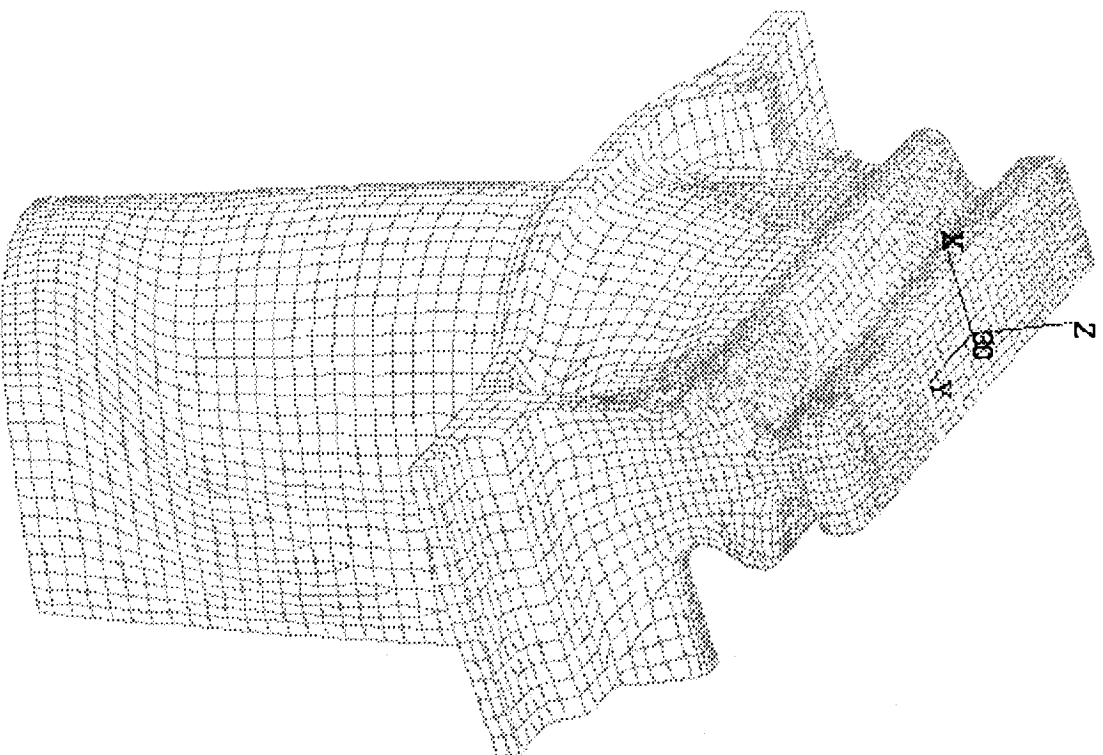Y axis pointing towards the second stage blade.

Figure 16. First Stage Blade FE Model and Casting
Coordinate System Coordinate System

Figure 19 Representative von Mises stress distribution results in the blade attachment region

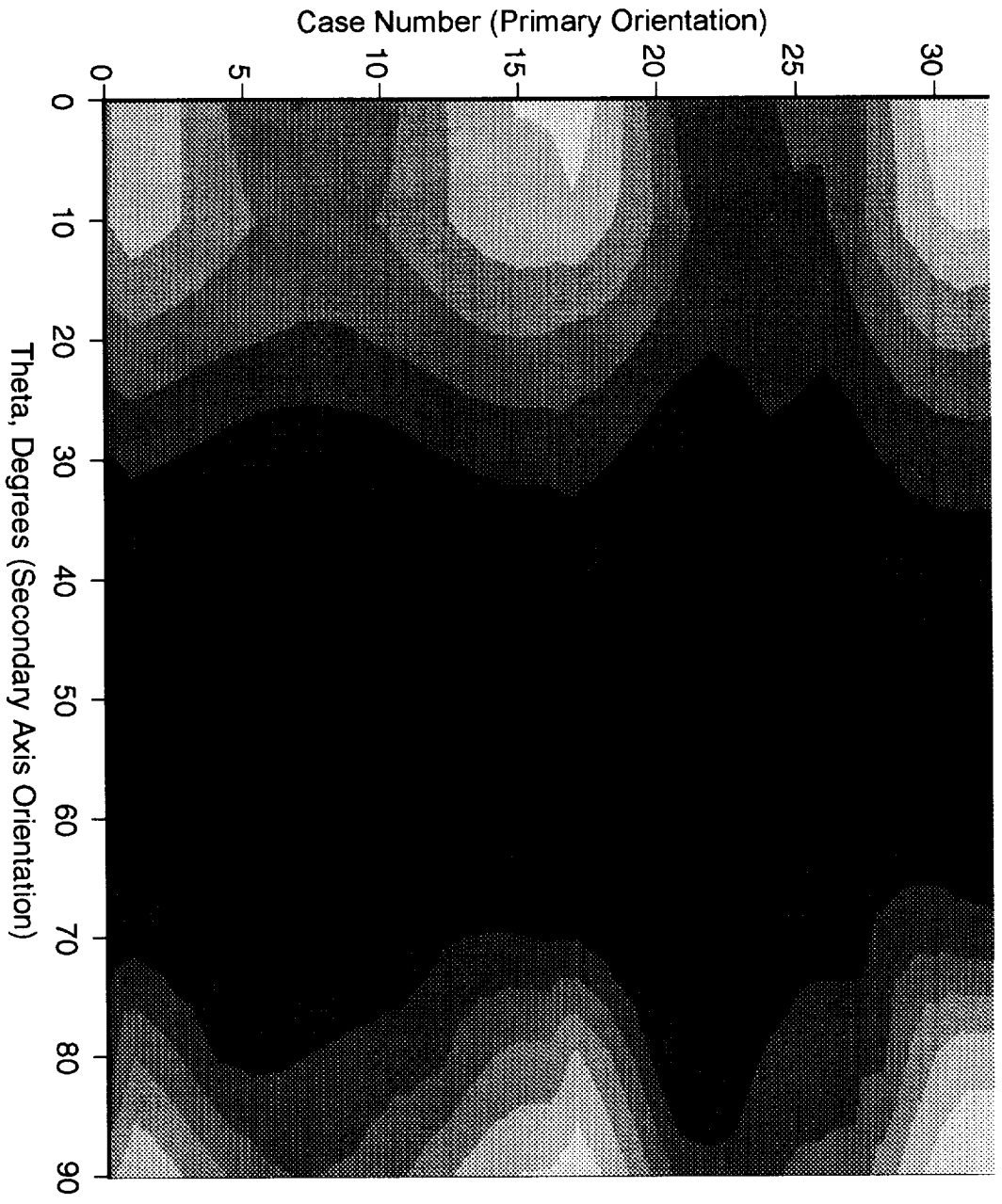0 Deg Primary, 22.5 Deg Secondary, Von Mises, Suction Side

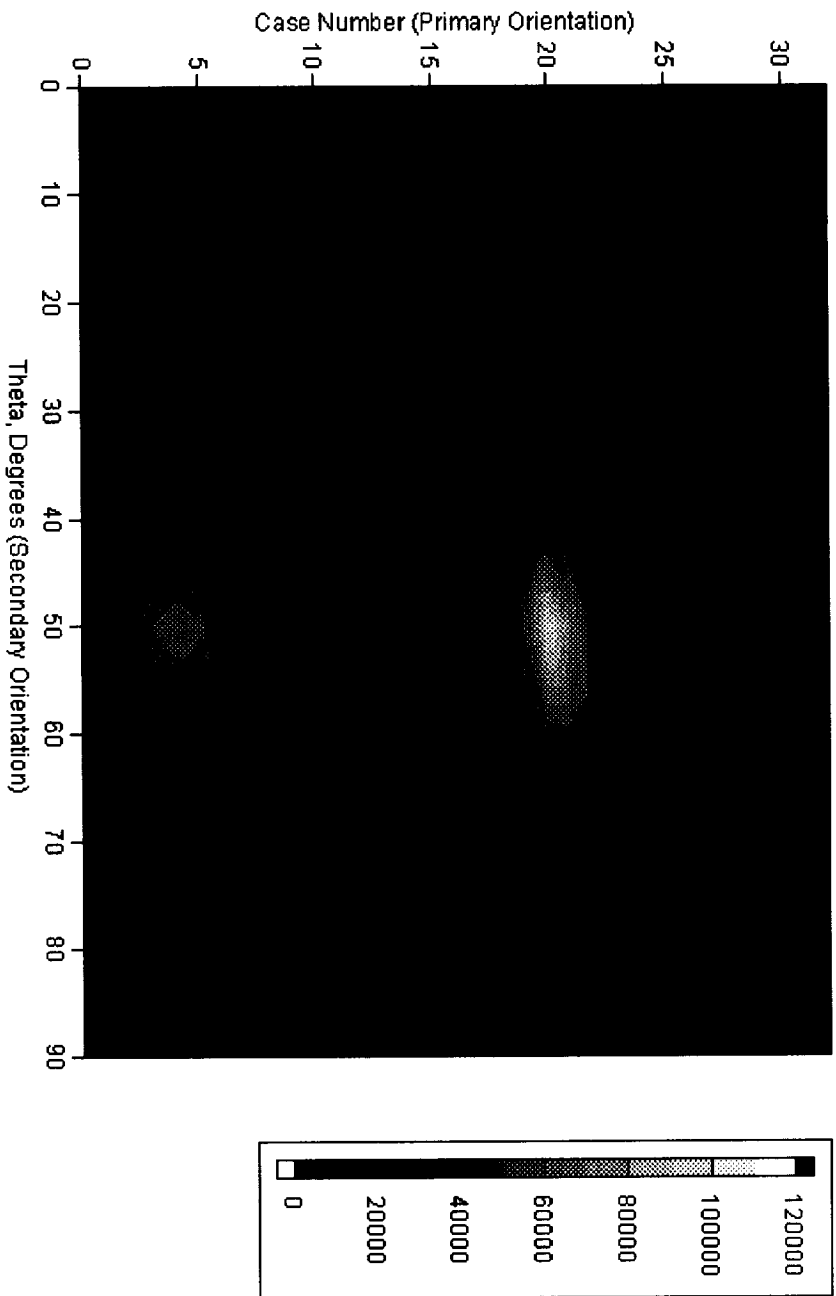**Fig. 20** Maximum Shear Stress Amplitude ($\Delta\tau_{max}$, ksi) Contour at the Blade Tip Critical Point

Fig. 21 Dimensionless Life Contours at the Blade Tip Critical Point